4 Part 3: Cooling Model

4.1 Background

Knowledge of the inner and outer temperatures of a block during cooling as functions of time should provide additional information which would be helpful in answering some of the questions posed in Part 2. To this end fully integrated partial differential equation solver software, FlexPDE[†††] was utilised to construct a numerical model predicting the surface and internal temperatures of a cooling slag block. The finite element model was constructed by Dr Johan Zietsman from Ex-Mente[‡‡‡] (a process modelling company) utilising FlexPDE version 5.0.13. The full model specification and all the inputs (such as slag properties, calculation procedure for heat transfer coefficients and pot dimensions) were provided by the author; the role of Dr Zietsman was to perform the actual coding of the model within FlexPDE. The accuracy of the numerically calculated solution via FlexPDE (version 5.0.13) was tested against the results of an analytical solution for a simple geometry. The numerical solution yield results similar to that of the analytical method. Details of this comparison are provided below. The model output was calibrated against actual internal slag block temperature measurements by adjusting the thermal conductivity of the slag (the only adjustable parameter, apart from boundary conditions such as cooling regimes, pouring temperature and block size). Subsequent verification of the model was done against actual surface temperature measurements and the thickness of the solidified shell after primary cooling.

4.2 Comparison of analytical and numerical solutions

Analytical solutions are not available for the situation considered here, with a fairly complex geometry, temperature-dependent materials properties, and time-dependent boundary conditions. For this reason, a numerical method had to be used to calculate the temperature changes during cooling of the blocks. However, to test the accuracy of the numerical solution calculated by FlexPDE, the "Neumann problem" (for which an analytical solution is available[29]) was used for comparison.

The Neumann problem considers a one-dimensional semi-infinite volume of material with a congruent melting point (T_f), which is originally at a uniform temperature (T_0) above the melting point. The face of the semi-infinite body is suddenly cooled (at time zero) to a temperature (T_s) which is below the melting point. The thickness of the solidified shell is then given by

$$X = 2\gamma\sqrt{\alpha_1 t}$$

where γ is a constant which is determined as mentioned below, and α_1 is the thermal diffusivity of the solid.

The temperature profiles in the solid ($x < X$) and liquid ($x > X$) are given by

---

[†††] See www.pdesolutions.com

[‡‡‡] See www.ex-mente.co.za

Solid: $T_1 = T_s + \dfrac{T_f - T_s}{\mathrm{erf}(\gamma)}\,\mathrm{erf}\left(\dfrac{x}{2\sqrt{\alpha_1 t}}\right)$

Liquid: $T_2 = T_o - \dfrac{T_0 - T_f}{\mathrm{erfc}(\gamma\sqrt{\alpha_1/\alpha_2})}\,\mathrm{erfc}\left(\dfrac{x}{2\sqrt{\alpha_2 t}}\right)$

where α_2 is the thermal diffusivity of the liquid, x is the distance from the cooled face, and *t* is time.

The value of γ is found by solving the following equation:

$$\frac{\exp(-\gamma^2)}{\mathrm{erf}(\gamma)} - \frac{k_2}{k_1}\sqrt{\frac{\alpha_1}{\alpha_2}}\,\frac{(T_o - T_f)\exp(-\alpha_1\gamma^2/\alpha_2)}{(T_f - T_s)\,\mathrm{erfc}(\gamma\sqrt{\alpha_1/\alpha_2})} = \frac{L\sqrt{\pi}}{c_1(T_f - T_s)}\gamma$$

In this expression, the subscript 1 refers to solid and 2 to liquid, k is the thermal conductivity, c is the heat capacity, and L is the heat of solidification.

For comparison of the analytical and numerical solutions, material properties which are similar to those of the real slag were assumed. These properties were as listed below:

C_1 (J/kgK)	C_2 (J/kgK)	L (J/kg)	ρ (kg/m^3)	k_1 (W/mK)	k_2 (W/mK)	α_1 (m^2/s)	α_2 (m^2/s)
900	1000	650000	4000	2	4	5.56×10^{-7}	1.0×10^{-6}

The initial temperature was taken as T_0 = 1550°C, the melting point as T_f =1520°C (for the numerical solution, the liquidus and solidus were set at 1530 ˚C and 1510 ˚C respectively), and the surface temperature as T_s = 100°C.

As in the numerical solution for the block, the apparent heat capacity was increased – by an amount of $L/(T_{liquidus} - T_{solidus})$ – between the solidus and liquidus temperatures, to include the heat of solidification. To avoid the discontinuities caused by the step changes in both the heat capacity and conductivity values, the SWAGE function of FlexPDE was used. This function generates a smooth transition from one value to another over a specified transition width (this width was taken to be one-tenth of the liquidus-solidus gap for the heat capacity, in this case). The SWAGE function also has smooth derivatives. The FlexPDE code of this example is given in section 5.4. As the code indicates, the surface temperature was not changed instantaneously in the numerical solution, but was ramped from the initial value to the required surface temperature over a period of 500 s; this (rather than an instantaneous change in temperature) was used to avoid numerical instability.

The temperature profile along this one dimensional domain for time increments starting at 1 hour, and for times double thus up to 128 hours are given in Figure 66. In this figure solid lines represent the results of the analytical solution while broken lines represent that of the FlexPDE solution. Figure 67 shows the shell thickness as calculated by both methods as a function of cooling time. Initially the numerical solution predicts a thicker shell that what the analytical solution does. This is a remnant of the initial difference in boundary conditions. After approximately 16 hours of cooling the two methods give comparable results.

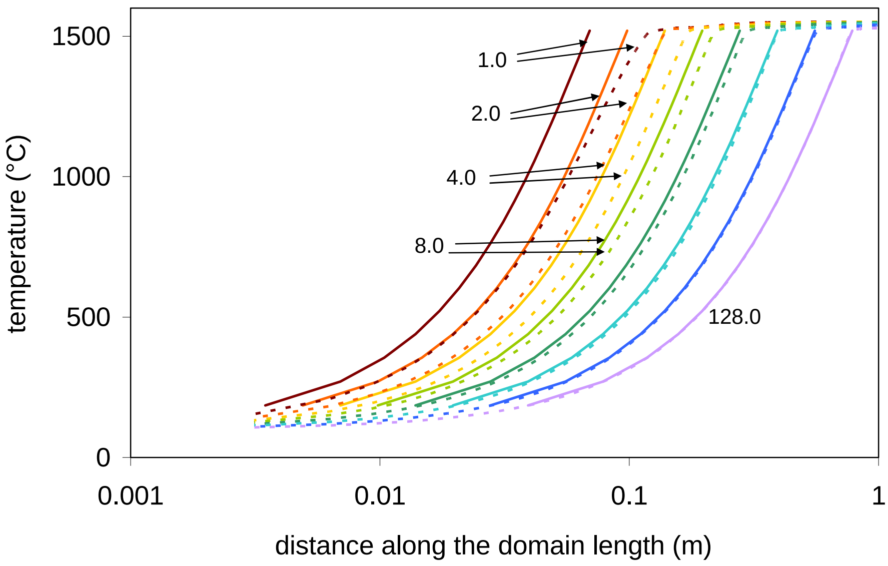

Figure 66 Temperature of the one dimensional semi-infinite body as a function of its distance during solidification (Neumann problem). Solid lines represent the results of the analytical solution, while broken lines represent the numerical results. The unit of the numbers is in hours.

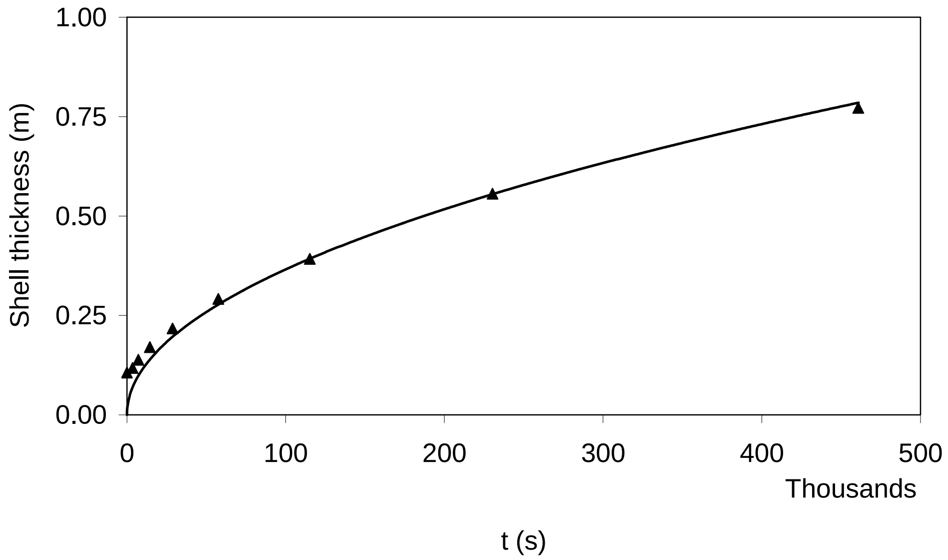

Figure 67 The shell thickness of a one dimensional semi-infinite shape solidifying from 1550 ˚C. The solid line represent the solution from the analytical method described above, while the triangles represent that of the numerical model as calculated by FlexPDE.

4.3 Model formulation

The following is a description of the model inputs, outputs, assumptions and material properties:

4.3.1 Requirements

In order to verify the model calculations on small scale 1 to 1.5 ton blocks, and to simulate large scale 17 to 20 ton blocks, the model provides for the following input:

Pot dimensions for the 1.5 ton pilot plant and 20 ton industrial plant pots

- Capacity (1.5 or 20 tons);
- Radius of the open end (0.523 or 1.175 m);
- Slope of the upper sidewall (15˚);
- Pot shell thickness (0.04 or 0.11 mm) and
- Pot temperature before tapping commences (25ºC).

Tap data

- Tap mass (ton);
- Tap temperature (ºC) and
- Slag FeO content (%).

Cooling conditions

- Time when the block is tipped out of the pot (with reference to the time at which the taphole was closed being time zero);
- Provision for several cycles of air and water cooling at adjustable durations;
- Water volumetric flow (m^3/hr);
- Drop diameter (mm) and
- Drop speed (m/s).

Other

- Ambient temperature and
- The time duration for which the model must perform the heat transfer calculations

The modelling software was able to provide calculated results in the following formats:

- Contour plots of isotherms within the block at a given time(s);
- Parameter (e.g. temperature) vs. time graphs for a named feature (e.g. horizontal surface) of the block;
- Parameter vs. position on a feature for a given time series.

4.3.2 Simplifications

- The pot shell is level with the upper surface of the block.

This is a valid assumption when the pot is filled up to capacity. Smaller taps do however result in the pot shell extending above the block. Such an extension of the pot will likely act as a fin for heat transfer: resulting in additional cooling at the corner between the horizontal and inclined surfaces of the block. However, given that conduction through the solidified solid slag shell is rate-determining (as the results show), the effect of this extra area for convection is small.

- The pot consists of a shell only, i.e. no provision was made for trunnions and feet.

  The additional mass and feet of the pot theoretically add to the heat extraction capacity of the pot. However, with the thermal resistance of the solidified slag as the rate limiting parameter (Section 4.10), the cooling of the block should not be different with or without this detail.

- The slag density is constant at 3.8 t/m^3.

  From visual inspections the slag is less dense closer to the (upper) horizontal surface in comparison with the bulk of the block: the internal structure closer to the horizontal surface typically contains gas holes which will result in a less dense material. This, combined with decrepitation occurring on the upper horizontal surface of the block during primary cooling, impacts notably on the accuracy of the heat transfer predictions (Section 4.8). However, in the absence of a detailed model of liquid flow and solidification shrinkage within the block during solidification, this effect could not be taken into account.

4.4 Energy balance

The primary partial differential equation to solve is:

$$\rho_{slag} Cp_{slag} \frac{dT}{dt} - k_{slag}\left(\frac{\partial^2 T}{\partial r^2} + \frac{\partial^2 T}{\partial z^2}\right) = 0 \tag{4}$$

Where ρ_{slag} is the density of the slag

Cp_{slag} is the heat capacity of the slag

$\frac{dT}{dt}$ is the rate of change of temperature at a given position

k_{slag} is the thermal conductivity of the slag

$\frac{\partial^2 T}{\partial r^2}$ and $\frac{\partial^2 T}{\partial z^2}$ are the second-order partial differentials of temperature in the r and z directions respectively. In a matrix format (as applied in the software calculations) the term $k_{slag}\left(\frac{\partial^2 T}{\partial r^2} + \frac{\partial^2 T}{\partial z^2}\right)$ translates to $\nabla \bullet \left(k_{slag} \nabla T\right)$ or in software recognizable nomenclature: $div\left(k_{slag} \times grad\left(T\right)\right)$.

The allowable error of the model is set at 0.1%. Should it be required the software refines the mesh in order to comply with this error limit.

In the instance of the two dimensional block, the numerical model was capable of utilising the heat capacity values (discussed in section 4.6.1) without the need of the SWAGE function as described in section 4.2. The heat conduction values were furthermore coded in as a linear function of temperature – hence also eliminating a potential discontinuity. As with the one-dimensional example, the heat of solidification was included by increasing the apparent heat capacity between the liquidus and solidus temperatures.

An energy balance check was run for a pilot scale size slag block. The results of this exercise are shown in Figure 68. The figure shows the total energy content of the cooling slag block, together with the total heat lost from the sides of the pot and the top surface of the ingot (up to a given time). The total of the energy content of the slag block and pot, and the integrated heat lost, is constant - demonstrating that the energy balance is maintained during the solidification simulation.

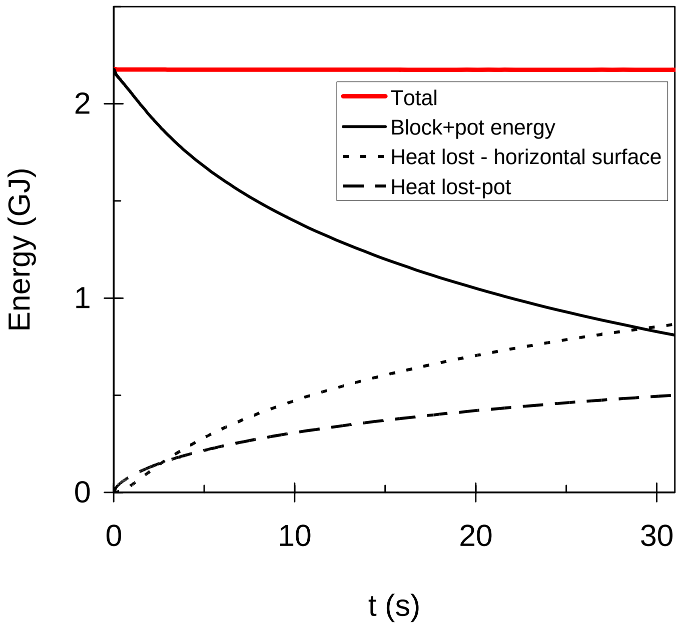

Figure 68 Results of an energy balance check conducted over a pilot scale size slag block.

4.5 Shape notations, dimensions and calculations

A sketch of a slice out of the block is shown in Figure 69. The important shape notations and their meaning are listed in Table 13.

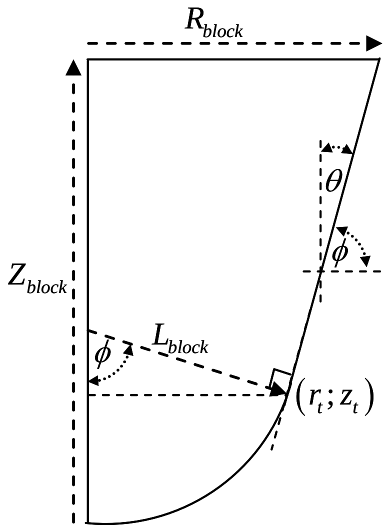

Figure 69 A sketch of the block illustrating the important shape notations.

Table 13 List of shape notations and their meaning used in describing the block shape.

Symbol	**Description**
R_{block}, Z_{block}	Maximum radius and full height of the slag block
L_{block}	Radius of the spherical section of the block
θ	Angle of upper pot shell with the vertical
ϕ	Angle of upper pot shell with the horizontal
r_t, z_t	Radius and height of the block where the conical and spherical sections meet

The following primary relationships were used to derive all shape dimensions:

- $V_{pot} = \dfrac{pot\ capacity}{slag\ density}$
- $V_{block} = \dfrac{tap\ mass}{slag\ density}$
- $r_t = L_{block} \cos\theta$
- $z_t = L_{block}(1 - \sin\theta)$
- Volume of a cone, $V_{cone} = \dfrac{\pi}{3} radius^2 \times height$
- Volume of a spherical cap, $V_{sphere} = \dfrac{\pi}{3} radius^3 \left(2 + \cos\phi\right)\left(1 - \cos\phi\right)^2$
- Area of a conical section, $A_{cone} = \pi\left(r_t + R_{block}\right)\sqrt{\left(Z_{block} - z_t\right) + \left(R_{block} - r_t\right)}$
- Area of a spherical cap, $A_{sphere} = 2\pi radius^2 \times \left(1 - \cos\phi\right)$

Hence, with the volume and radius of the pot, V_{pot} R_{pot} respectively as input parameters, the radius of the spherical section of the block is calculated from:

$$L_{block} = \left(\frac{V_{pot} - \frac{\pi R_{pot}{}^{3}}{3\tan\theta}}{\frac{-\pi\cos\theta^{3}}{3\tan\theta} + \frac{\pi}{3}\left(2+\cos\phi\right)\left(1-\cos\phi\right)^{2}} \right)^{\frac{1}{3}} \tag{5}$$

The block radius and height is calculated from:

$$R_{block} = \left(\frac{3\tan\theta}{\pi}\left(V_{block} - V_{sphere}\right) + r_t^{3} \right)^{\frac{1}{3}} \tag{6}$$

$$Z_{block} = \frac{\left(R_{block} - r_r\right)}{\tan\theta} + z_t + L_{block} \tag{7}$$

With the shape specified according to the above equations FlexPDE5 constructs a mesh with triangular nodes. The mesh is adapted with consistency checks over the solutions of the partial differential equations. When required the node size and/or time step is reduced. This typically occurs close to the solidification front, because of the sharp change in enthalpy with temperature. An example of a mesh configuration showing original and reduced size nodes are shown in Figure 70.

To accommodate the change in the boundary conditions of the system (cooling of a combined slag block and pot vs. cooling of a slag block alone, after tipping of the slag block from the pot), two FlexPDE codes were constructed. The first provided for a volume consisting of two materials (the block and pot) each with its own material properties. In this instance heat transfer from the pot and horizontal block surface to the surroundings was by natural air cooling. The second file provided for the block on its own. Heat transfer to the surroundings could be selected as either natural air cooling or water cooling. Data transfer from the first to the second file was established through the TRANSFER statement of FlexPDE. This statement enables full data sharing between different FlexPDE runs. The boundary conditions for both these systems are discussed in section 4.7. The full code of both FlexPDE files is given in section 5.5.

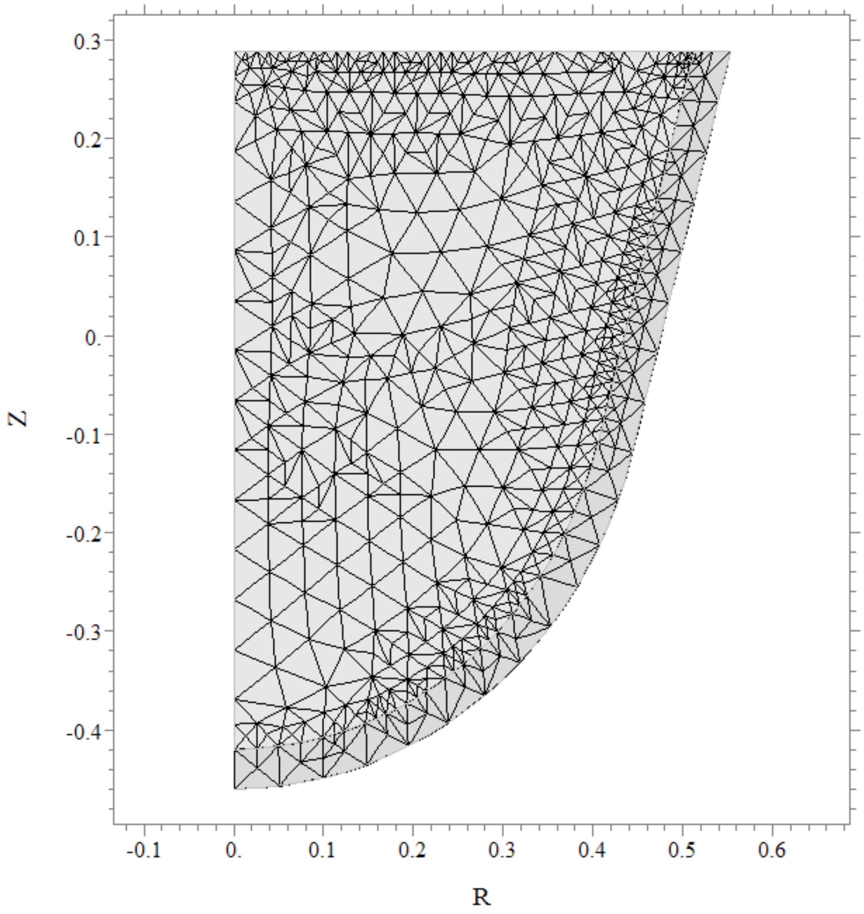

Figure 70 Example of the mesh configuration for the slag block (Z and R are in metre). Areas of denser node configurations are shown where FlexPDE reduced the node size to remain within the accuracy tolerance of 0.1%.

4.6 Material definitions

4.6.1 Slag thermodynamic properties

The liquidus and solidus temperatures of the slag, and the change in enthalpy of the slag with temperature, are important inputs into the heat transfer model. These properties were estimated by means of FactSage[17], and approximated with simple mathematical relationships (based on the FeO content of the slag as the independent variable). The procedure followed is outlined below.

4.6.1.1 **Choice of slag compositions**

A database of 112 full plant slag analyses was obtained (elemental composition determined by X-ray fluorescence, and Ti^{3+} by titration). These analyses are shown in Figure 71. The mass percentages of the other components varied approximately linearly with FeO content, for FeO levels ranging from just above 6% to more than 18%. These analyses were grouped together by FeO content, and an average analysis per FeO range was obtained (a valid approach, given the approximately linear variation of slag analysis with FeO content). These average analyses are listed in Table 14. Note that these analyses are normalised to 100%; small amounts of other impurities (K_2O, V_2O_3, Nb_2O_3 and ZrO_2) - making up less than 1% of the slag - are hence neglected.

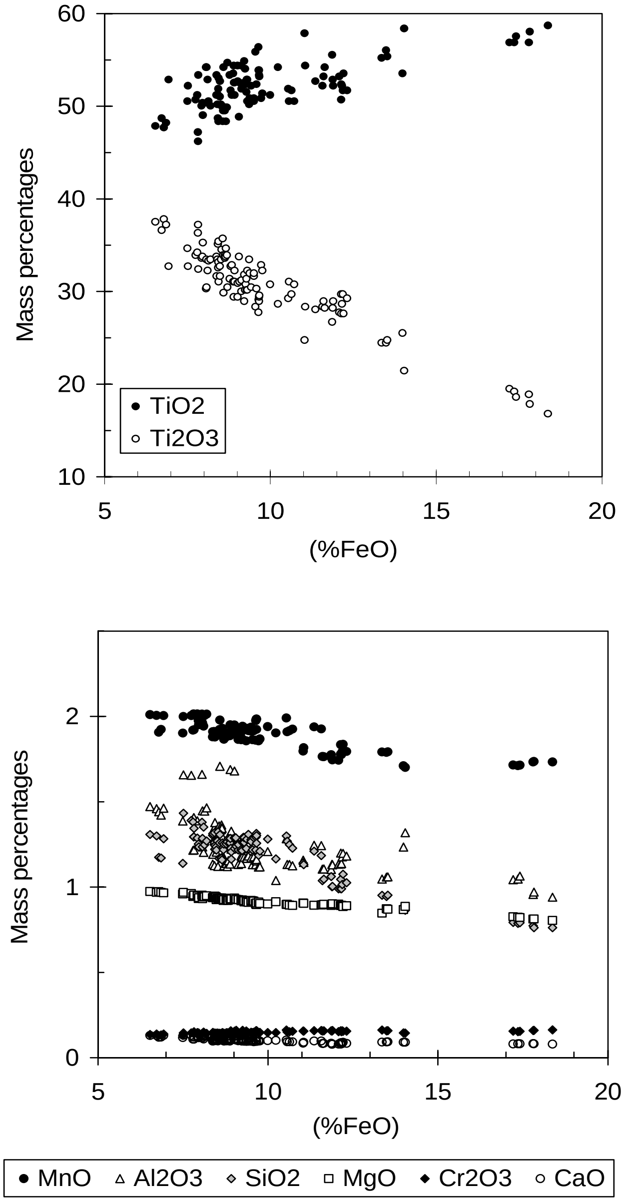

Figure 71 Analyses (mass%) of industrial plant slags.

4.6.1.2 Thermodynamic properties

FactSage was used to predict the changes in phase composition and enthalpy with temperature, for each of the eight slag compositions. The following phases (from the "FT oxid" database of FactSage were considered):

- Solutions: SlagA, pseudobrookite (karrooite), $Ca_3Ti_2O_7$-$Ca_3Ti_2O_6$ and perovskite
- Stoichiometric solid phases: all relevant oxides, except the Ti_nO_{2n-1} Magnéli phases.

In addition to suppression of the Magnéli phases, ilmenite and spinel solid solutions were also not considered. This was to ensure stability of pseudobrookite down to room temperature (in line with the observed persistence of pseudobrookite in the actual solidified slag).

Typical changes in the liquid fraction and enthalpy for one of the slags (no. 4 in Table 14) are given in Figure 72. The continuous curves give the temperature dependence as predicted by FactSage. This shows a sharp decrease in liquid fraction just below the liquidus, with a tail extending to lower temperatures. For the purpose of the model, this relationship was approximated by a linear one, matching the calculated profile at the liquidus temperature and at 80% solidification (indicated by T_{20} in the figure). The effective solidus temperature ("$T_{solidus}$" in Figure 72) was found by extending the linear relationship to zero liquid.

Table 14 Average compositions of eight groups of slags from the full plant dataset; each group spans a specific range of FeO contents.

No.	FeO	Ti_2O_3	TiO_2	MnO	Al_2O_3	SiO_2	MgO	Cr_2O_3	CaO
1	6.86	38.05	49.09	2.00	1.48	1.26	0.99	0.14	0.13
2	8.05	34.21	51.75	2.01	1.42	1.33	0.97	0.15	0.12
3	8.85	33.09	52.34	1.94	1.31	1.27	0.95	0.15	0.11
4	9.71	31.28	53.38	1.96	1.21	1.29	0.93	0.15	0.10
5	10.85	30.28	53.33	1.95	1.17	1.25	0.92	0.16	0.10
5	12.14	28.93	53.69	1.83	1.18	1.07	0.91	0.16	0.09
7	13.89	24.51	56.59	1.78	1.16	0.93	0.88	0.16	0.09
8	17.98	18.83	58.55	1.76	1.02	0.79	0.83	0.16	0.08

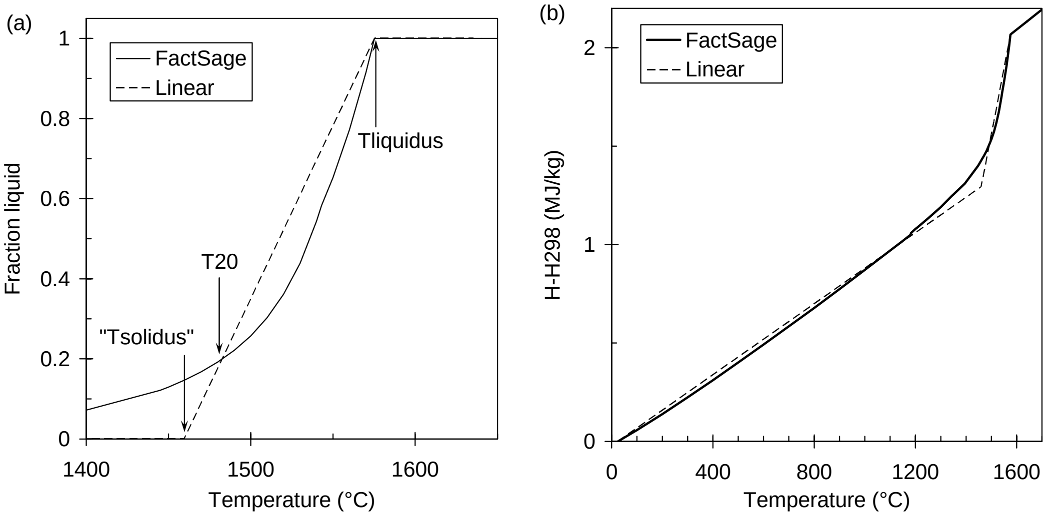

Figure 72 Predicted effect of temperature on (a) the fraction liquid and (b) the enthalpy (relative to that of solid slag at 298 K) of slag no. 4. The broken line gives the linear approximation which was used as model input.

A linear enthalpy relationship was similarly used as model input. This matched the calculated enthalpy at the liquidus temperatures, and in the fully liquid region (where FactSage reports a constant heat capacity). In the solid region, the linear relationship matched the calculated trend at 298 K and at 1373 K (1373 K is just below the generally observed true solidus); all enthalpies were expressed relative to that of the solid at 298 K. The estimated solid enthalpy at the extrapolated solidus temperature, "$T_{solidus}$", was found by extrapolating this 298 K – 1373 K linear relationship for the solidified slag; the enthalpy was also assumed to change linearly (between that of the solid slag and that of the liquid slag) over the temperature range $"T_{solidus}" - T_{liquidus}$. Hence the effective heat capacity between $"T_{solidus}"$ and $T_{liquidus}$ is given by equation (8) (with temperatures in ˚C). These linear approximations are given in Table 15. The fitted relationships are given in equations (9) to (14).

$$Cp^{solid-liquid} = \left(\frac{H_{298}^{liquid} + Cp^{liquid}\left(T_{liquid} - 25\right) - Cp^{solid}\left("T_{solid}" - 25\right)}{T_{liquid} - "T_{solidus}"} \right) \tag{8}$$

Table 15 Parameters of linear approximations to thermodynamic properties, and fitted relationships.

No.	$T_{liquidus}$	$"T_{solidus}"$	Cp^{solid}	Cp^{liquid}	H_{298}^{liquid}
	(°C)	**(°C)**	**(J/kgK)**	**(J/kgK)**	**(MJ/kg)**
1	1601.17	1470.34	903.60	1024.32	0.5014
2	1586.19	1451.36	903.73	1020.45	0.4989
3	1581.56	1463.56	902.75	1018.46	0.4957
4	1575.25	1459.53	901.88	1016.48	0.4916
5	1570.31	1453.99	900.64	1015.02	0.4867
6	1564.82	1450.26	898.56	1012.52	0.4819
7	1553.52	1440.63	896.46	1007.64	0.4745
8	1537.42	1427.74	891.26	1001.96	0.4510

$$T_{liquidus} = 0.2351(\%FeO)^2 \text{-} 11.24(\%FeO) + 1664.1 \qquad °C \tag{9}$$

$$"T_{solidus}" = 0.0364(\%FeO)^2 - 4.845(\%FeO) + 1502.7 \qquad °C \tag{10}$$

$$Cp^{solid} = -0.0314(\%FeO)^2 - 0.4042(\%FeO) + 908.51 \qquad J/kgK \tag{11}$$

$$Cp^{liquid} = 0.0561(\%FeO)^2 - 3.3668(\%FeO) + 1044.3 \qquad J/kgK \tag{12}$$

$$H_{298}^{liquid} = -139.51(\%FeO)^2 - 1086.1(\%FeO) + 515805 \qquad J/kg \tag{13}$$

$$f_{liquid} = \min\left(\max\left(\frac{T \text{ - } "T_{solidus}"}{T_{liquidus} \text{ - } "T_{solidus}"}, 0 \right), 1 \right) \tag{14}$$

The conductivity of titania slag is incorporated in the model as a linear function of temperature (equation (15)). The values of the constants a and b were determined by fitting the model results to the actual measurements from thermocouples inserted into the slag blocks directly after tapping. This work was conducted during Campaign 10 on the pilot plant. This calibration procedure is discussed in detail in section 4.8.

$$k = aT + b \tag{15}$$

4.6.2 Pot thermodynamic properties

The heat capacity of the cast steel pot was assumed to be constant at 465 W/kg˚C[30], while the thermal conductivity of the pot was expressed as a function of temperature (equation (16)). Both these values are representative of a 0.5%C steel. To test this approach, the heat losses from the outer surface of the pot are shown by the black line in Figure 73. The black line in Figure 73 represents the heat losses from the outer surface with a constant heat capacity; while the brown line represents model results with the heat capacity of the pot equal to that of pure iron - and varying with temperature (Figure 74). The heat losses from the block surface to the pot differed at most by 20,000 J for the full and simplified expressions for pot heat capacity. This difference furthermore occurs only over the first hour of cooling. Hence, seen relative to the magnitude of energies present in the block during the first hour of cooling (1 kg of slag at 1600˚C has an energy content in the order of 2 MJ - Figure 72), this difference was treated as negligible and the heat capacity of the steel pot was set at a constant value.

$$k_{pot} = -0.03488\left(T_{slag}^{surface}\right) + 59.1 \tag{16}$$

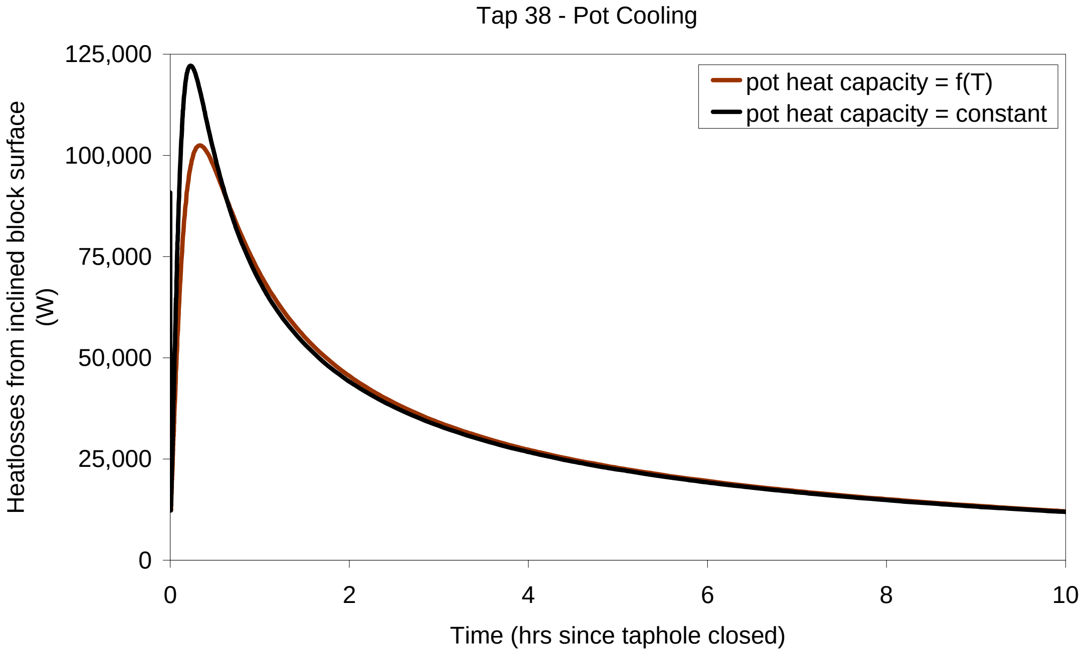

Figure 73 Heat losses from the outer pot surface during solidification of a 1,365 kg block. The black line represents model results with constant heat capacity of the pot, while the brown line represents model results where the pot heat capacity is that of pure iron.

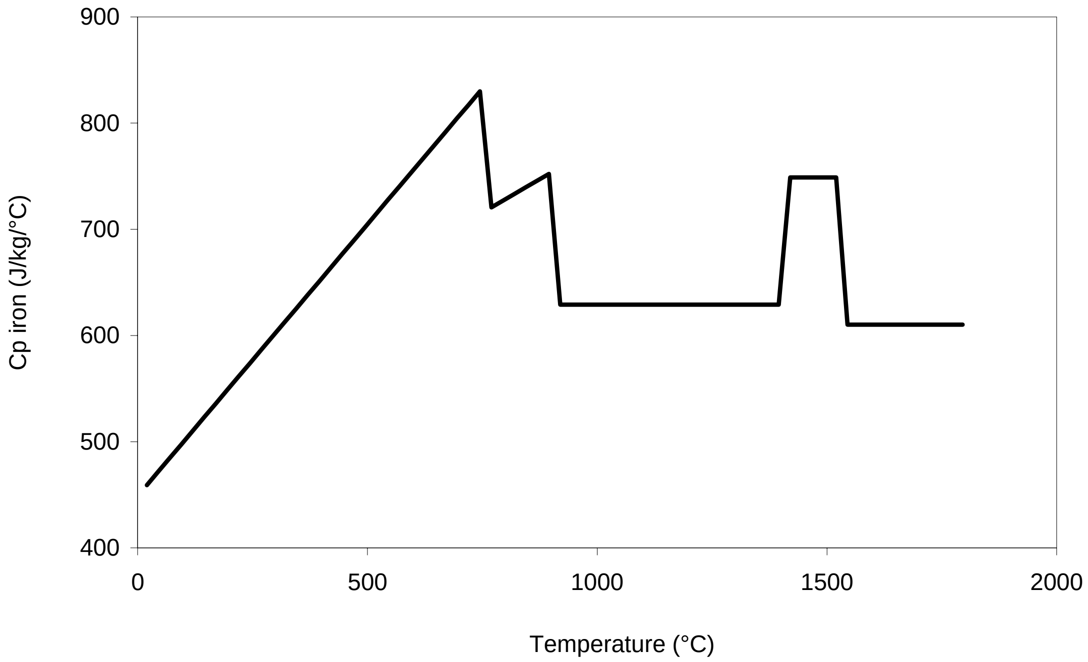

Figure 74 Heat capacity of pure iron.

4.7 Boundary conditions

4.7.1 Contact coefficient between the block and pot surfaces

A thermal contact resistance arises between the slag block and the pot, and this may affect the solidification process by lowering the rate of heat transfer from the block to the pot. It is hence important to evaluate whether this contact resistance is as significant here as it is in the solidification of other materials in metal moulds, for example aluminium alloy castings[31] and partially crystalline polymers.[32]

The thermal contact resistance arises because the solid surfaces (of the pot and the slag block) are not in perfect contact, but rather contact one another at asperities.[33] Conductive heat transfer between the solids is limited to the small area of the asperities; the conduction area hence depends on the roughness of the two surfaces, and the pressure on the surfaces. In parallel, conduction occurs through the layer of gas (air in this case) between the surfaces.

The temperature drop across the contact resistance is then given by:

$$\Delta T = AR_c \frac{q}{A}$$

where ΔT is the temperature drop, A the apparent interfacial area (that is, not just the contact area at the asperities), and $\frac{q}{A}$ is the heat flux across the interface.

The contact resistance represents the parallel contribution of conduction through the asperities, and conduction through the air gap:

$$\frac{1}{R_c} = \frac{1}{R_{asperities}} + \frac{1}{R_{gap}}$$

The resistance of the air gap is given simply by

$$AR_{gap} = \frac{L}{k_{air}}$$

where L is the average width of the air gap, and k_{air} the average thermal conductivity of the air in the gap.

For conforming solid surfaces (that is, solid surfaces in good macroscopic contact, as is the case here for the block in the conical pot, one expression for the contact resistance of the asperities is:[33,34]

$$AR_{asperities} = \frac{\sigma/m}{\left[1.25k_s\left(\frac{P}{H_c}\right)^{0.95}\right]}$$

where σ is the average roughness of the surface (in m), m is the average slope of the asperities, k_s is the harmonic mean of the thermal conductivities of the contact surfaces (defined below), P is the pressure (in Pa) on the interface, and H_c is the Vickers hardness (in Pa) of the surface.

The value of m can be estimated from the surface roughness (for σ in μm) as follows:[33]

$$m = 0.076\sigma^{-0.52}$$

The harmonic mean thermal conductivity is given by

$$\frac{1}{k_s} = \frac{1}{2}\left(\frac{1}{k_{pot}} + \frac{1}{k_{block}}\right)$$

These expressions were used to estimate the size of the contact resistance.

In this application, the effect of the contact resistance is expected to be small, for two reasons. First, the conical shape of the pot ensures good contact with the solid surface of the block: if temperature changes cause the block to shrink (or the pot to expand), the block simply descends in the pot. Second, the low thermal conductivity and large size of the block imply a low heat flux through the block-pot contact area, and large solidification times. Solidification times are several hours (pilot-scale blocks) to tens of hours (plant-scale blocks); in comparison, the solidification times of the aluminium alloy and polymer castings quoted above are of the order of minutes. The low heat flux through the block-pot contact implies a small temperature drop across the thermal contact resistance.

The approach to evaluation of the effect of the contact resistance was twofold. First, the expressions as given above were used to estimate the thermal contact resistance. Second, temperature measurements were conducted on the pot during solidification of a pilot-scale block.

To estimate the contact resistance, a simplified conical block was considered, as illustrated in the figure below. An upper-bound estimate of the force normal to the conical interface between the pot and the block (F_N) is obtained if it assumed that the pot-block surface is frictionless. The vertical force (F_V) must equal the weight of the block, hence F_N is given by:

$$F_N = \frac{\rho V g}{\sin\theta}$$

where ρ is the density of the slag, V the volume the block, g acceleration due to gravity, and θ the half-angle of the apex of the cone.

The volume of the cone is given by

$$V = \frac{\pi r^2 h}{3}$$

The pressure across the interface is then given by

$$P = \frac{F_N}{A_{cone}} = \frac{g\rho h}{3}$$

In deriving this relationship, the expressions for the area of the cone $A = \pi r\left(r^2 + h^2\right)^{0.5}$ and $\sin\theta = \frac{r}{\left(r^2 + h^2\right)^{0.5}}$ were used.

Since the contact resistance decreases if the contact pressure (P) increases, the largest contact resistance is expected for the pilot-scale block, with the smallest height.

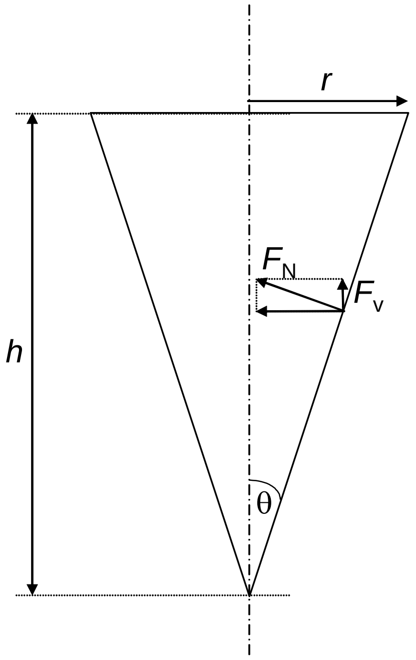

Figure 75 Simplified conical pot and block, which was used to estimate the thermal contact resistance.

Estimated values of the contact resistance, based on these expressions, are given in Table 16. In these expressions, the surface roughness (σ) is taken to be 100μm; microscopic inspection of solidified slag surfaces indicates that this is an upper bound on the actual roughness. The thermal conductivity of air is taken to be 0.04 W/mK, which is a reasonable average for the gap temperatures during solidification. The average width of the air gap was taken to be equal to the surface roughness. The results in the table indicate that conduction across the interface is expected to be dominated by conduction through the air, with a total thermal resistance of 0.0025 m^{2}K/W, for a 100 μm gap.

This estimated thermal resistance is small compared with the thermal resistance of the solidifying shell of the slag block; a thermal resistance of 0.0025 m^{2}K/W (equal to the estimated contact resistance) is given by a slag layer which is 2.5 mm thick (assuming a thermal conductivity of 1 W/mK). The conclusion that the contact resistance is small compared with the thermal resistance of the solidified slag holds even for a much larger pot-block air gap. For example, an air gap of 1 mm is equivalent (in thermal resistance) to a solidified slag layer with a thickness of 25 mm, which is also small compared with the size of the block.

Table 16 Input data used to estimate contact resistance for pilot-scale block, with estimated resistances.

ρ_{slag} (kg/m^3)	k_{slag} (W/mK)	k_{steel} (W/mK)	k_s (W/mK)	k_{air} (W/mK)	σ (μm)	m	h (m)	P (Pa)	H (kg/mm^2)	H (GPa)
4000	1	50	1.96	0.04	100	0.83	0.6	7848	150	1.47

Thermal resistance of asperities: (m^{2}K/W)	Thermal resistance of air gap: (m^{2}K/W)
5.0	0.0025

Based on these considerations, the thermal contact resistance is expected to play an insignificant role in solidification of the block. Note that radiative heat transfer was not considered in this analysis, since radiation effects can be neglected for temperatures below 900 K[35] (which is typical for the pot for most of the cooling period). Any role of radiation would decrease the contact resistance, in any case.

The above conclusion was tested by comparing pilot-plant measurements of the pot temperatures with model predictions. For these model predictions, the effect of the contact resistance was neglected. If the contact resistance were significant, the pot temperature would hence be significantly lower than the predicted values. The results of this comparison (conducted during campaign 10) are shown in Figure 76, with the model predictions shown as lines, and measured temperatures as data points. The locations of the thermocouples are shown in Figure 85; the three thermocouples were located between the open end of the pot (black line in Figure 76) and the transition point between the spherical and conical sections of the pot (brown line in Figure 76). The temperature measurements from thermocouples 2 and 3 fit neatly between these two lines. The deviation between the readings from thermocouple 1 and the model predictions of the pot open end edge could be explained by the model assumption that the pot height is equal to that of the block. This differs from the actual situation where the pot edge extends above the slag block. As mentioned earlier, this edge could act as a cooling fin leading to lower temperatures in the upper ring of the pot which is exposed to natural air cooling.

The accuracy of the model predictions hence confirms that omitting a contact resistance between the block and pot does not impact on the accuracy of the model results.

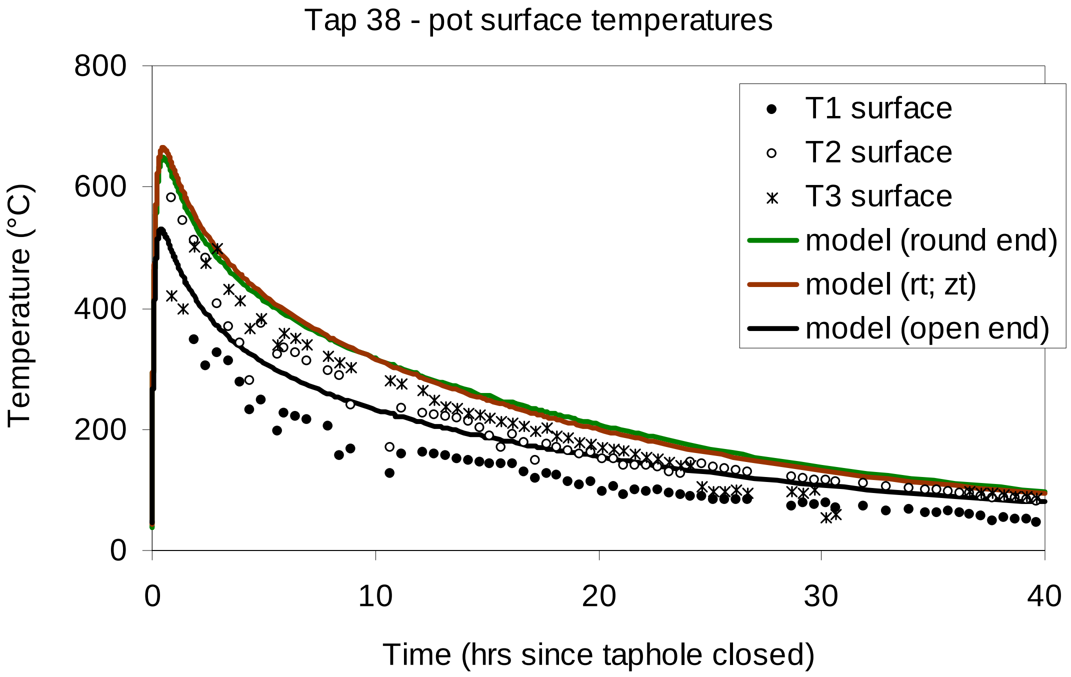

Figure 76 Pot surface temperatures as predicted by the cooling model (lines). Symbols indicate surface measurements derived from actual temperature measurements within the pot shell.

4.7.2 Contact coefficient between the block and ground surface

During secondary cooling the horizontal surface of the block faces the ground. With the hot downward-facing surface effectively suppressing natural air convection, this boundary condition was modelled via a contact resistance as per equation (17). This resistance depended on the thermal conductivity of air, k_{air}; average height of the air gap between the block and ground surfaces, $\overline{d}$, and the radiation coefficient, h_{rad} which is calculated as per equation (21). While the width of the air gap between the block and ground surfaces does vary, an average gap height of 10 mm was assumed. Comparisons of the heat losses from the horizontal surface of the block after tipping where the average air gap varied between 5 and 50 mm showed block cooling to be fairly insensitive to the size of the air gap (Figure 77). Subsequent model runs were conducted assuming an average gap height of 10 mm.

$$h_{contact} = \frac{k_{air}}{\overline{d}} + h_{rad} \tag{17}$$

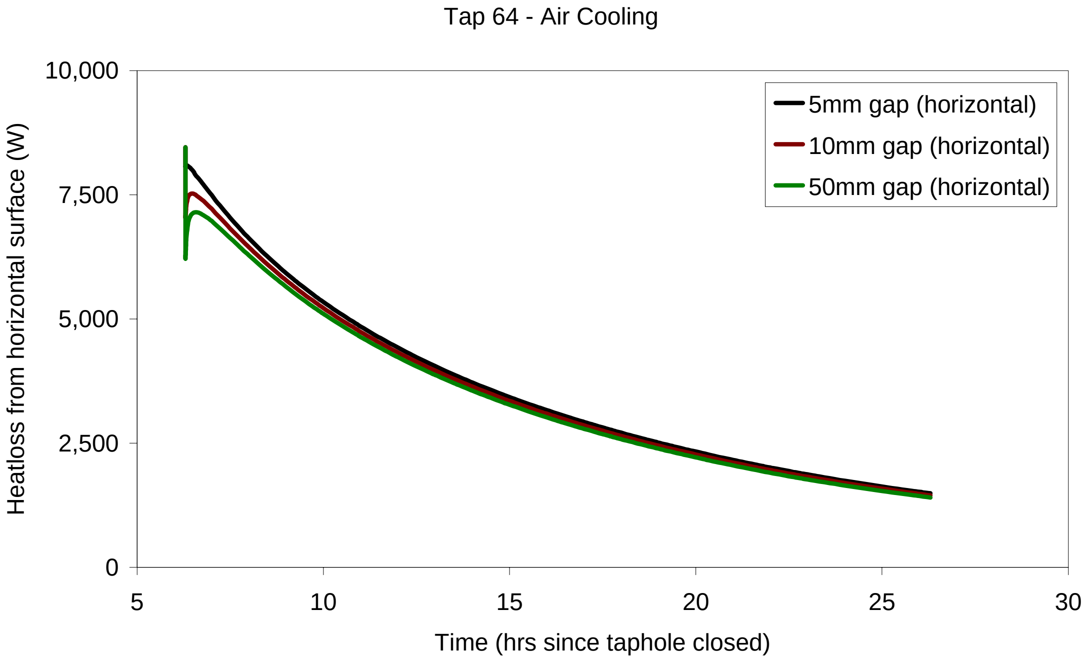

Figure 77 Heat losses from the horizontal downward-facing surface of the block during secondary cooling. The different lines show the insensitivity of heat losses to the assumed height of the air gap between the block surface and ground.

4.7.3 Natural convection in air

During primary cooling in the pot, the pot outer surface and horizontal block surface are exposed to natural convection in air. During this time the pot surface acts as an inclined heated surface facing downwards. After being tipped out of the pot, the conical and spherical surface of the block acts as an inclined heated surface, facing upwards. The convection heat transfer coefficient for the above conditions was calculated from correlations and constants provided by Holman[36] and summarised below.

The average heat transfer coefficient, $\overline{h_{conv}}$ is calculated from equation (18).

$$\overline{Nu}_f = C\left(Gr_f \Pr_f\right)^m = \frac{\overline{h_{conv}} L}{k_f}$$

so that (18)

$$\overline{h_{conv}} = \frac{k_f}{L} C\left(Gr_f \Pr_f\right)^m$$

Where k_f and $\Pr_f$ are the thermal conductivity and Prandtl number of air at film temperature respectively.

L is the characteristic dimension of the shape. For the horizontal surface of the block $L = \dfrac{surface\ area}{surface\ perimeter} = \dfrac{1}{4} diameter$. For the pot surface facing downwards (during primary cooling and the block surface facing upwards (after the block is tipped out of the pot) $L = \dfrac{\cos\theta}{Z_{block}}$.

The Grashof number at film temperature, Gr_f, is calculated from

$$Gr_f = \frac{g\,\beta\left(T_{surface} - T_\infty\right) L^3}{\upsilon^2}$$

with $g = 9.81\ \mathrm{m.s^{-2}}$

β = inverse of the average film temperature in K (19)

$T_{surface}$ = surface temperature

T_∞ = temperature of the surroundings

υ = kinematic viscosity of air at film temperature

For the block surface facing downwards, the Grashof number is modified to:

$$Gr_f = Gr_f \cos^2\theta \tag{20}$$

The values for the constants C and m are as per Table 17.

Table 17 Constants used for calculation of the heat transfer coefficient as per equation (18).

	Horizontal		**Vertical**	
Grashof number	$\leq 8\times10^6$	$> 8\times10^6$	$\leq 10^9$	$> 10^9$
C	0.54	0.15	0.59	0.10
m	$\frac{1}{4}$	$\frac{1}{3}$	$\frac{1}{4}$	$\frac{1}{3}$

The total heat transfer coefficient (Figure 78) is calculated from the sum of the convection component as described above and the radiation component as per equation (21).

$$h_{rad} = \sigma\varepsilon\left(T_{surface}^{\;2} + T_{\infty}^{\;2}\right)\left(T_{surface} + T_{\infty}\right) \text{ with } T \text{ in K} \tag{21}$$

where $\sigma = 5.669\text{x}10^{-8}$ in $\text{W/m}^2\text{K}^4$, and

$\varepsilon = 0.8$

The resulting heat transfer coefficients for the horizontal and inclined surfaces are shown in Figure 78. At higher temperatures the contribution of the radiation coefficient (brown line in Figure 78) becomes increasingly predominant.

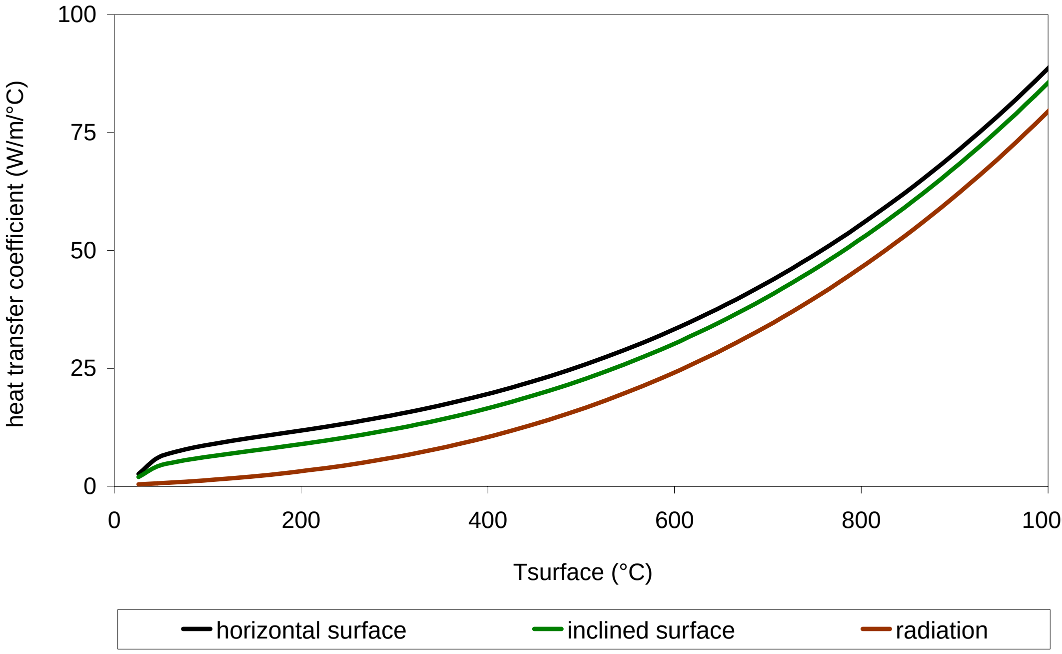

Figure 78 Heat transfer coefficients for natural cooling in air.

4.7.4 Forced spray water cooling

The heat transfer conditions in spray water cooling are considered similar to the known heat transfer conditions of pool boiling[37,38]. The heat transfer regimes of pool boiling are illustrated in Figure 79: at high surface temperatures – above the Leidenfrost point –film boiling prevails. In this regime a vapour blanket prevents direct contact between the surface and liquid and effectively limits heat transfer. On further cooling of the surface to below the Leidenfrost point, the heat transfer gradually increases up to the point of critical heat flux. This increase in heat transfer is driven by breaking up of the vapour film resulting in partial contact between the liquid and surface. Below the critical heat flux, nucleate boiling determines the rate of heat transfer; and at temperatures below the point of incipience of nucleate boiling, natural convection prevails. The shape of the boiling curve for a given heat transfer situation depends (amongst others) on the surface roughness, water temperature and spray hydrodynamics. For the purposes of the block cooling model the heat transfer coefficient for spray water cooling was derived from the work of Klinzing et al[37], utilising the original expressions of Mudawar[38].

Heat transfer coefficients calculated for varying volumetric flows, drop speeds and drop diameters are shown in Figure 80. A list of expressions used to calculate the heat transfer coefficient is given in Appendix 5.4 Within the tested range of parameters, the heat transfer coefficient is sensitive to the volumetric water flow rate, but insensitive to the drop diameter. Increasing drop speed moves the Leidenfrost temperature to higher values. It is interesting to note that the lowest heat transfer coefficients are experienced at surface temperatures in the range where decrepitation typically occurs.

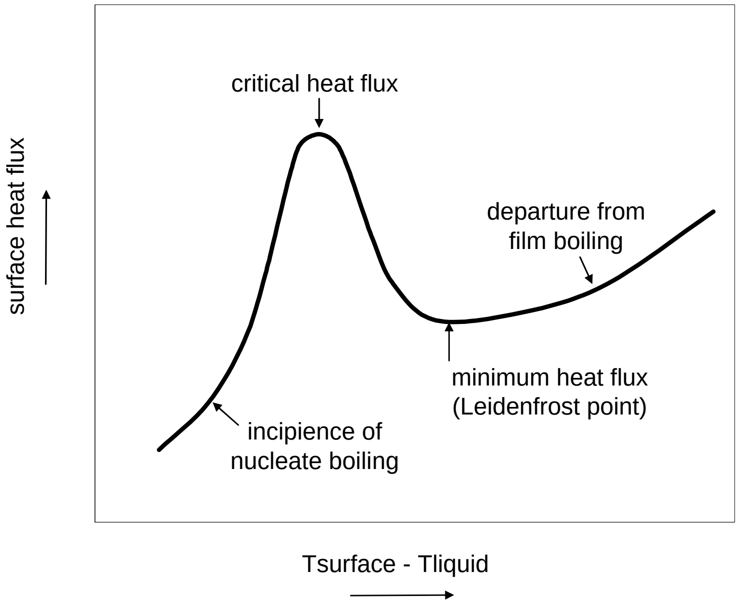

Figure 79 Boiling curve associated with quenching of a hot surface in a stagnant pool.[37,38]

The model-predicted surface temperatures of block 42 (campaign 9) are shown in Figure 81 with varying water volumetric flow and drop speed values. The black line represents the average surface temperature of a narrow (±10mm) vertical area along the inclined surface of the block as measured with a stationary thermal camera. The surface temperatures appear to be insensitive to the spray water parameters. Note that the periodic temperature increases are reheating of the block surface when the spray water was turned off. With the spray water turned on, the water flow was clearly sufficient to quench the surface temperature to close to the water temperature (hence the insensitivity to spray water parameters).

The change in heat transfer coefficient between water and air cooling is shown in Figure 82. (During periods of water cooling on a given surface, the heat transfer coefficient of air is ignored for that surface – during air cooling the water-cooling heat transfer coefficient is not used.) While the heat transfer coefficient in natural air cooling is usually around 10 W/m^2°C, it increases by two to three magnitudes during spray water cooling (note the logarithmic scale of heat transfer coefficient on the right hand side of the graphs in Figure 82).

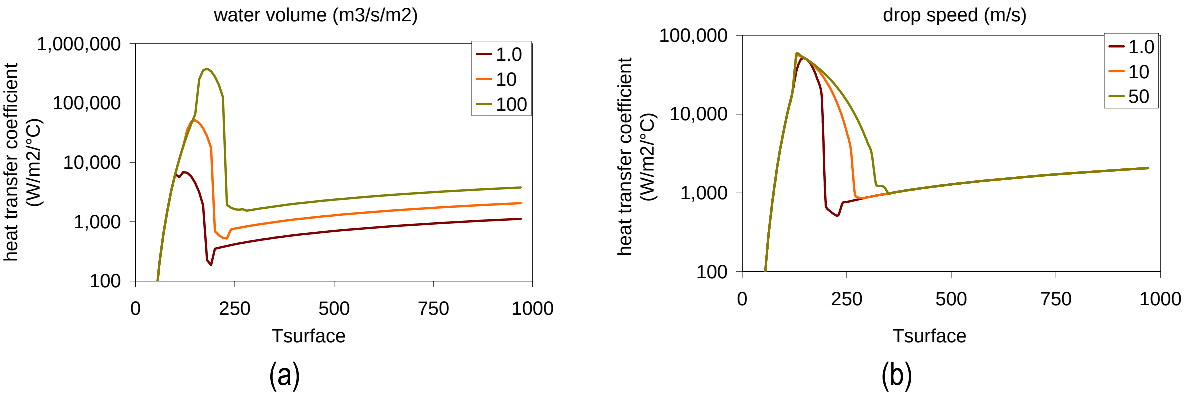

(a) (b)

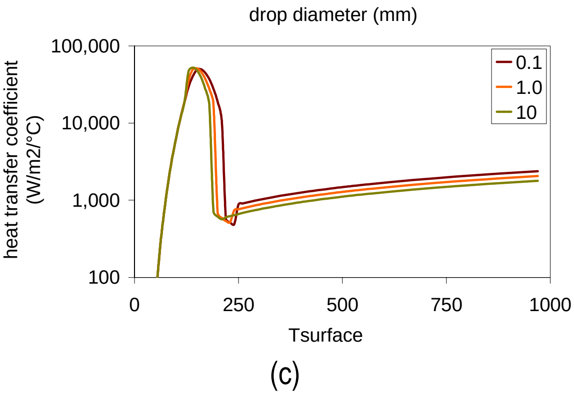

(c)

Figure 80 Heat transfer coefficients for cooling in water with varying (a) volumetric water flows (b) drop speeds and (c) drop diameters. Surface temperatures are in °C.

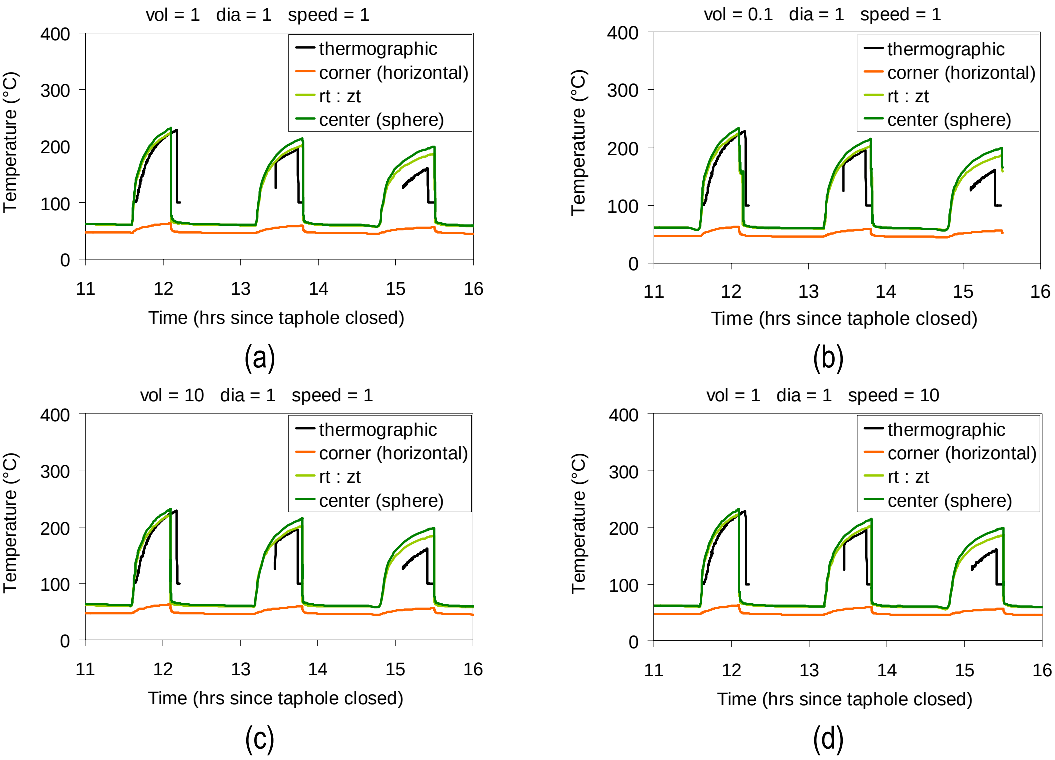

Figure 81 Model-predicted results for block surface temperatures for different of water volumetric flow rates and drop speeds.

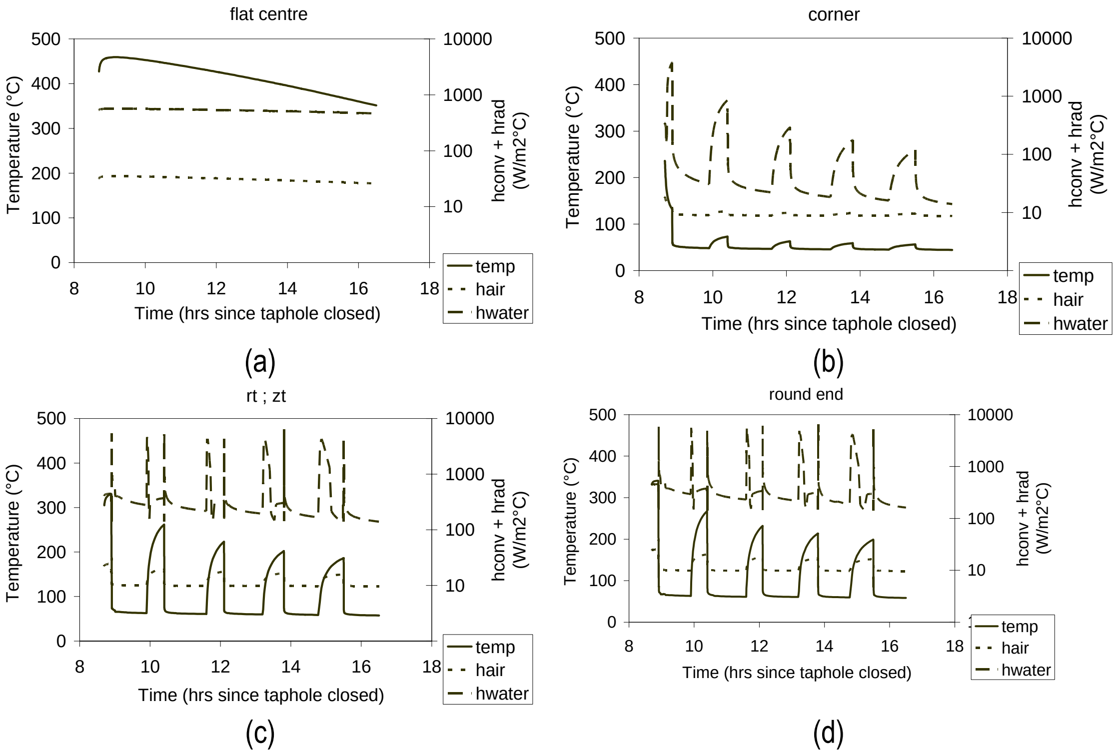

Figure 82 Surface temperature and heat transfer coefficients for intermittent water cooling at four positions on the block. “Flat centre” is the centre of the horizontal surface, “corner” is the corner between the horizontal and inclined surfaces of the block, “$r_t : z_t$” is the join on the surface of the spherical and conical block volumes, and “round end” is the centre of the round end of the block.

4.8 Model calibration

During the 10th 3 MVA pilot-plant ilmenite-smelting campaign thermocouples were inserted into two blocks directly after tapping. These thermocouples were positioned as shown in Figure 83 and Figure 85. The configuration of the three centre line thermocouples is shown in Figure 84. The Alsint tube (alumina thermocouple sheath) was inserted into the silicon carbide tube and both these tubes were closed at the bottom end. Three 0.25 mm (wire diameter) type S-thermocouple and sheath combinations were positioned within the Alsint tube at different heights as shown in Figure 85. The thermocouples marked A, B and C denote the thermocouples which were inserted down the centre line of the block; while those marked 1, 2 and 3 were double thermocouples inserted into holes drilled into the shell of the pot. The thermocouple inserted off-centre into the block (Figure 83) failed and hence no data was obtained from it.

The tap information and slag composition of the two taps are given in Appendix 5.8.

The thermal conductivity of titania slag is not a well known number – especially not as a function of temperature[39]. The model results were hence calibrated to the actual thermocouple measurements by adjusting the slag thermal conductivity. The accuracy of the fit was determined by calculating the sum of the errors as per equation (22). The RMS error proved to be smallest with the thermal conductivity expressed as a linear function of temperature: $k = aT + b$. The relationships between the choice of constants a and b and the resulting RMS errors are shown in Figure 86 and Figure 87 for taps 37 and 38 respectively. The best-fit values for the respective coefficients for each of the thermocouples are shown in Table 18, while the best fit k-value for each thermocouple is plotted in Figure 90. The uppermost thermocouple inserted into tap 37 (T_A) deviated substantially from the close grouping of the other five thermocouples. From visual observations the upper layer of the slag block typically has a very porous structure. Hence, with thermocouple T_A being located high up in the block (Figure 85) it was likely positioned within this porous upper layer where the thermal conductivity is apparently dominated by the porous slag structure. The best fit k-value for this layer seems to be 0.5 W/m.˚C, much lower than elsewhere in the block. As mentioned earlier, the effects of the porous structure of the upper layer were not included in the model; the thermal conductivity everywhere in the slag block was hence described by equation (23).

$$RMS\ error = \sqrt{\frac{\sum\left(T^{t}_{actual} - T^{t}_{model}\right)^{2}}{n}} \tag{22}$$

$$k_{slag} = 0.00175T + 0.3 \text{ where } T \text{ is in } °C \tag{23}$$

Figure 83 Photograph of a slag block and pot directly after thermocouples were inserted into the block. For support the refractory tubes were inserted into the slag through slots in a steel channel which was placed horizontally over the pot edge.

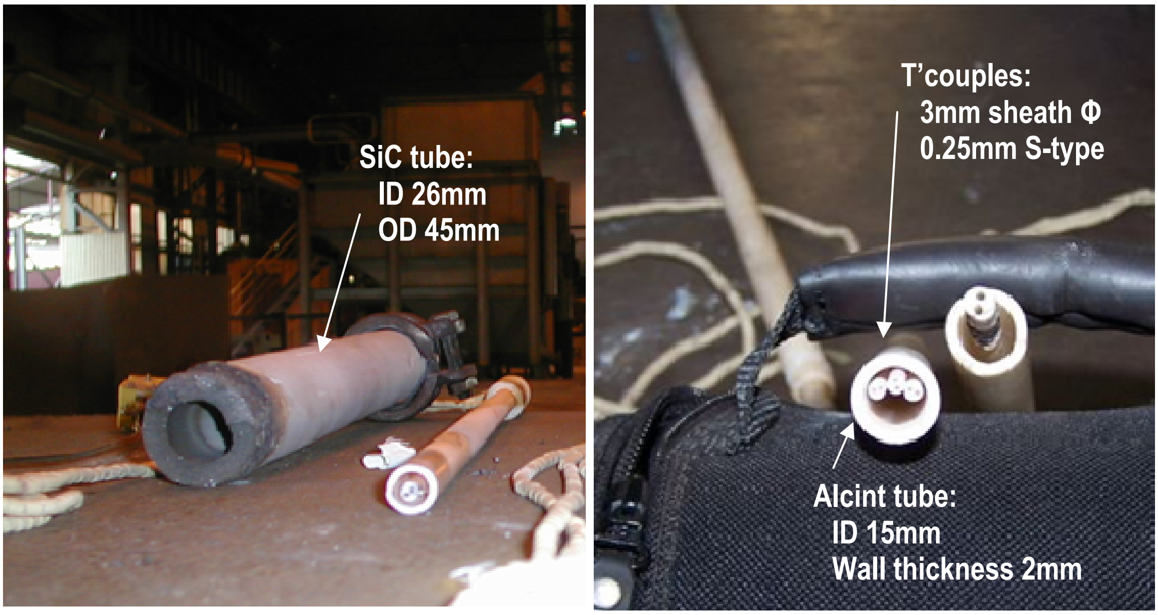

(a) (b)

Figure 84 Photograph showing the configuration of the thermocouples which were inserted into the slag blocks.

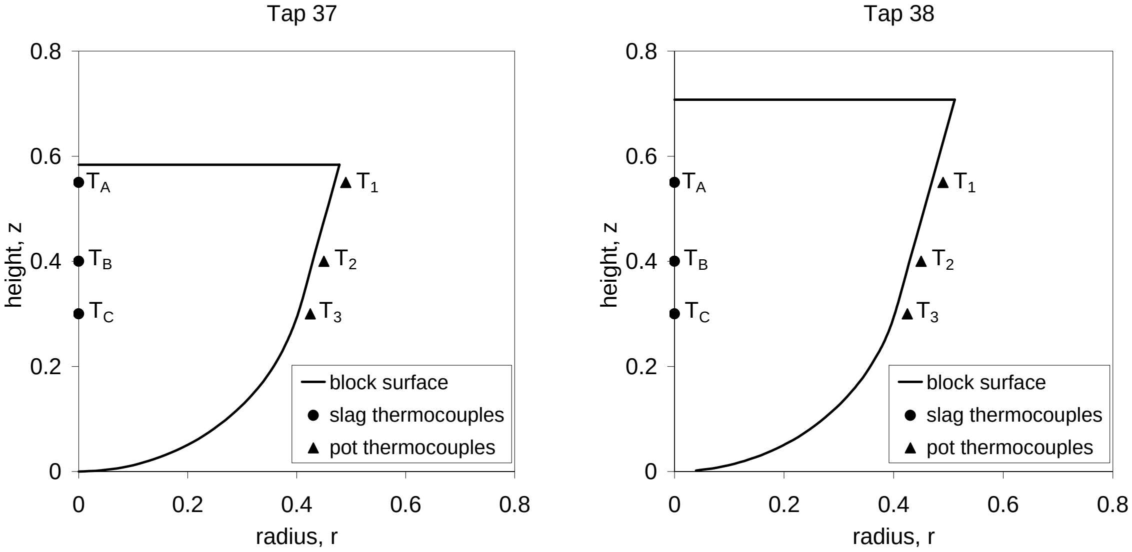

(a) (b)

Figure 85 Thermocouple positions for blocks 37 and 38 tapped during Campaign 10. Alphabetic subscripts denote thermocouple positions inserted into the slag, while numeric subscripts denote positions of thermocouples inserted into the pot shell.

Table 18 Best-fit values for coefficients a and b for each of the thermocouples inserted into the slag blocks (expression: $k_{slag} = aT + b$).

	Thermocouple	a (W/m°C^2)	b (W/m°C)
Tap 37	A	0.0000	0.50
	B	0.0019	0.30
	C	0.0018	0.30
Tap 38	A	0.0017	0.30
	B	0.0018	0.35
	C	0.0016	0.20
Model		0.00175	0.3

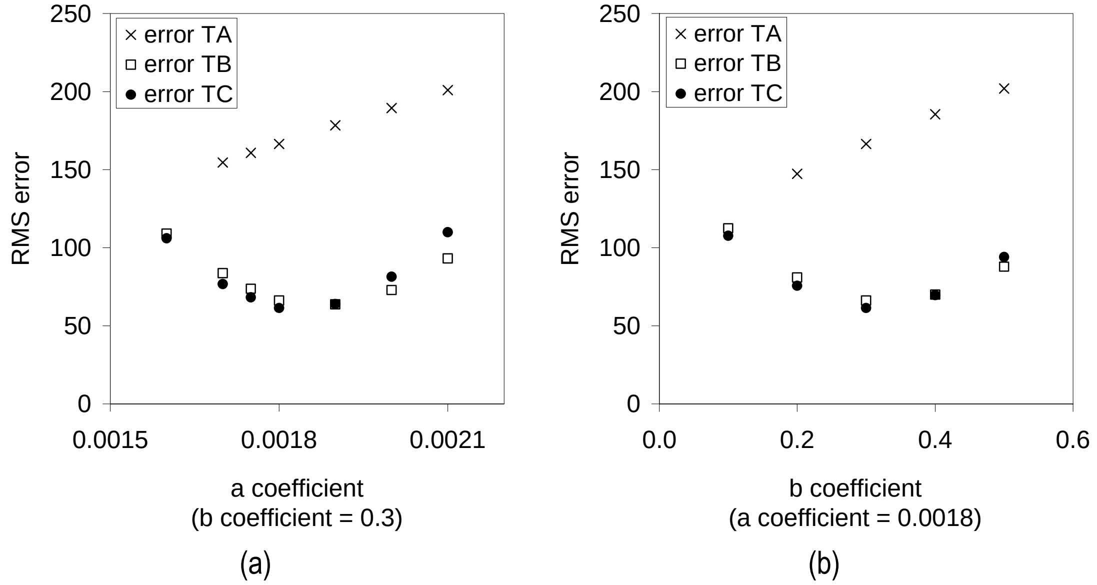

(a) (b)

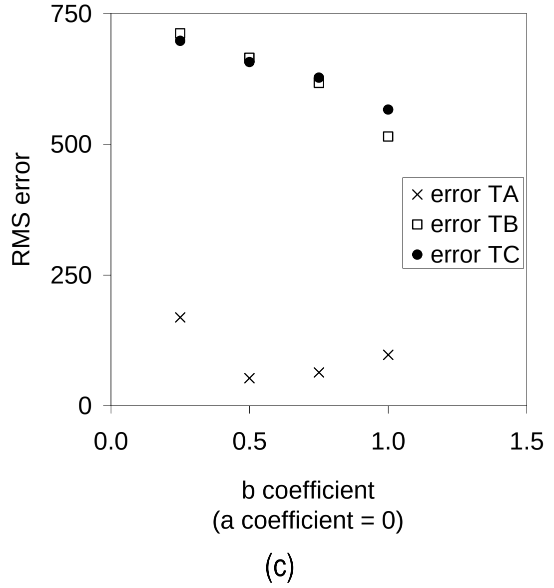

(c)

Figure 86 RMS error (in ˚C) of actual vs. model predictions for slag temperatures within tap 37.

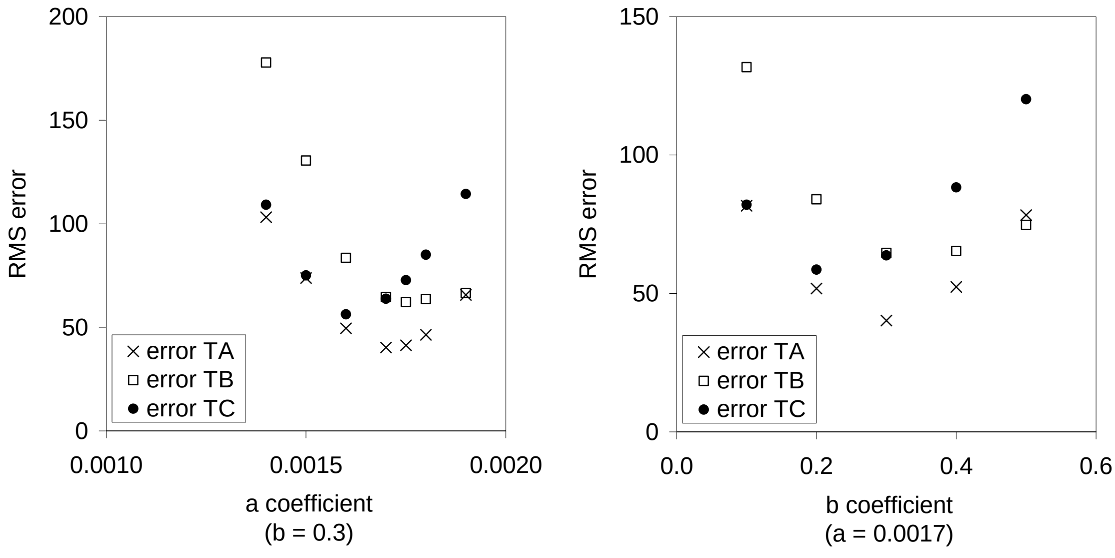

(a) (b)

Figure 87 RMS error (in ˚C) between actual temperature measurements and model predictions for tap 38.

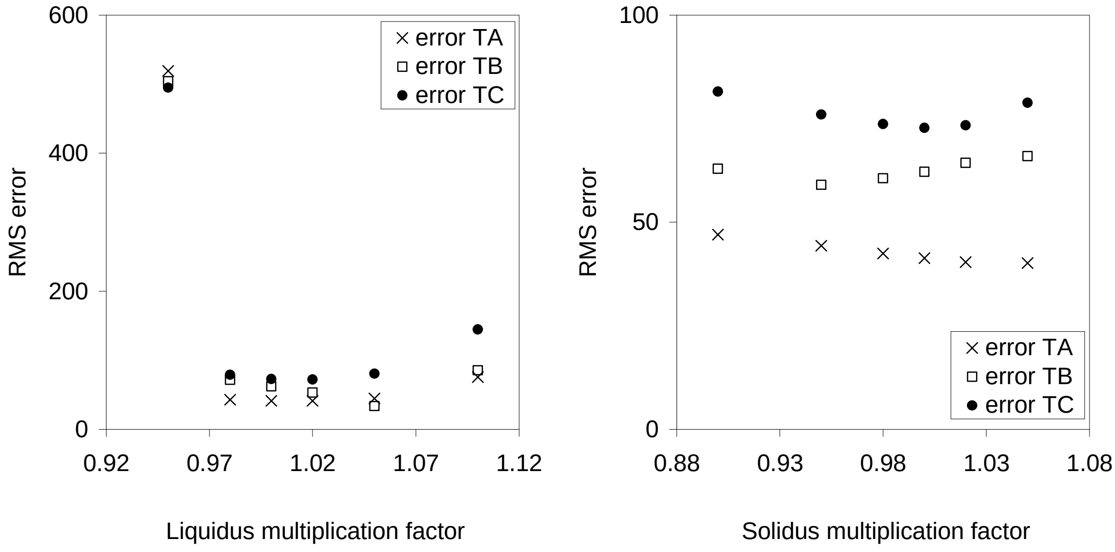

(a) (b)

Figure 88 RMS errors (in ˚C) between the actual and model predicted slag temperatures with $k_{slag} = 0.00175T + 0.3$. (a) Liquidus and (b) solidus temperatures were varied with ± 2% and ± 5%.

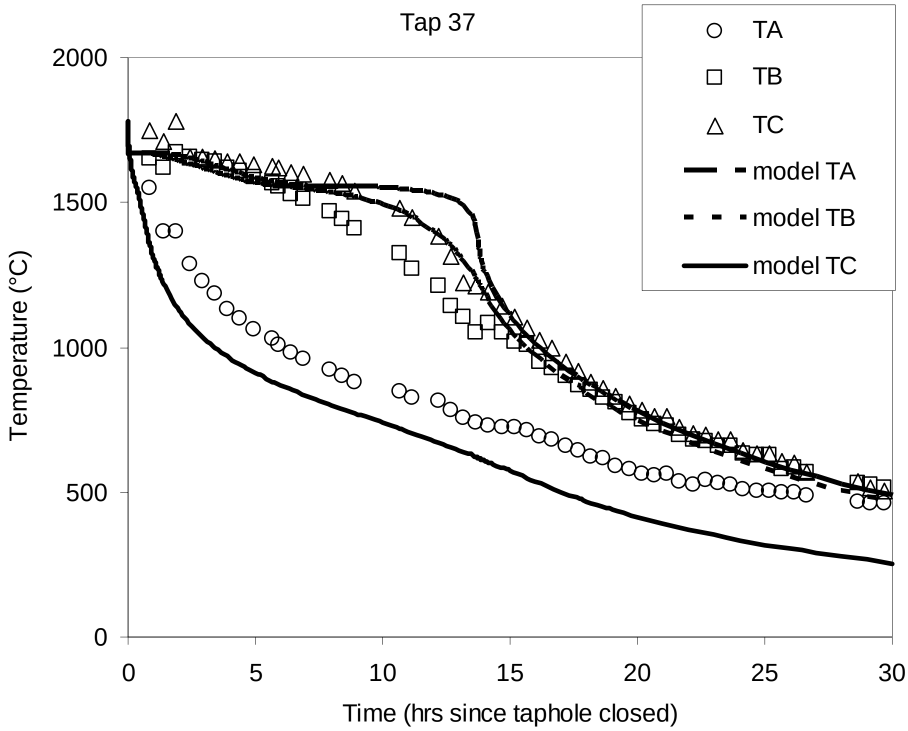

(a)

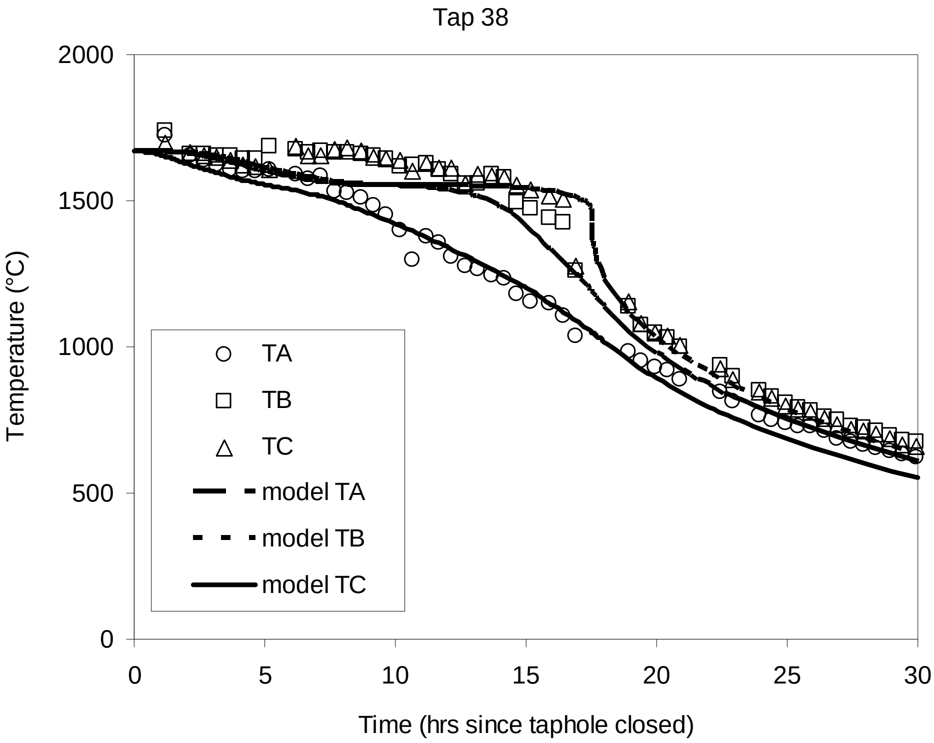

(b)

Figure 89 Internal slag temperatures for (a) tap 37 and (b) tap 38. Lines indicate model predictions, while symbols represent actual temperature measurements (k=0.00175T+0.3).

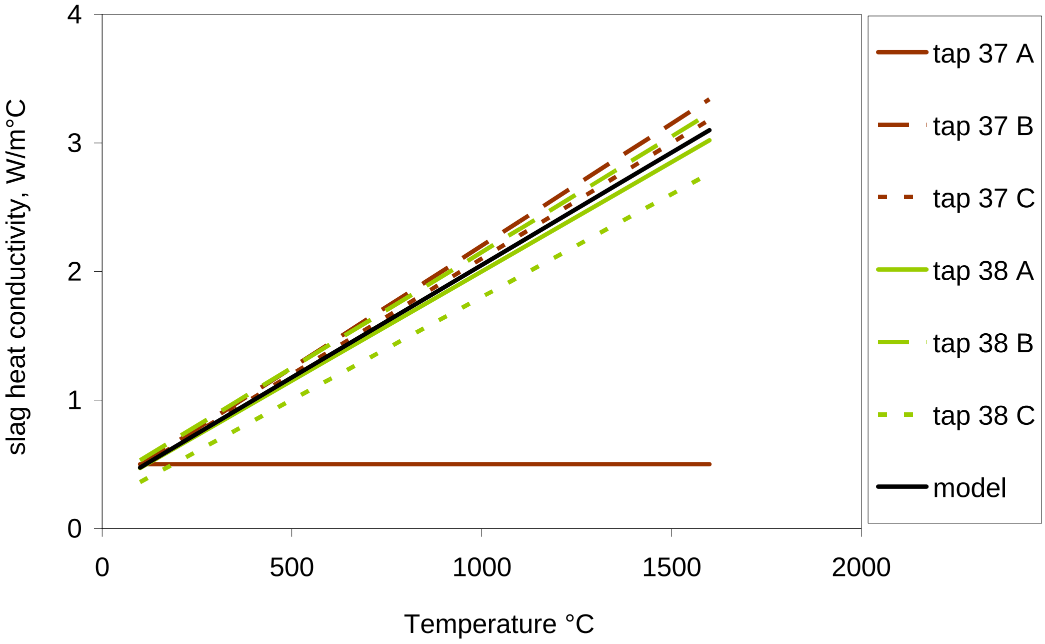

Figure 90 Best fit k-values for taps 37 and 38. For modelling purposes the k-value was expressed as given by the solid black line.

The fitted values of the thermal conductivity of the solidified slag – increasing from approximately 1 to 3 W/mK, for a temperature increase from 200°C to 1500°C – is in line with what is expected for this type of material. This is illustrated by Figure 91, which compares the fitted thermal conductivity with those of natural rocks, and synthetic pseudobrookite. The main mechanism of heat conduction in these materials is phonon conductivity (diffusion of lattice vibrations), for which the expected relationship is an inverse proportionality of the thermal conductivity to absolute temperature.[40] However, the presence of anisotropy and disorder in real structures cause deviation from this relationship.[40] The increase in the fitted slag thermal conductivity with temperature is in agreement with the observation that natural rocks with thermal conductivities below 2 W/mK at room temperature show increases in thermal conductivity with increasing temperature.[40]

The values for the M_3O_5 materials in Figure 91 were recalculated from thermal diffusivity values reported by Siebeneck et al.[44,45], using the average heat capacity over the range of temperatures (using enthalpies from FactSage), the room-temperature values for density[41,42], and the thermal expansion coefficients.[44,45] The strong hysteresis in the thermal conductivity of these materials (that is, the measured values differ upon heating and cooling) was ascribed to microcracking of the material. Microcracking arises because of significant anisotropy of the thermal expansion coefficients: for Fe_2TiO_5 these coefficients are $\alpha_a=0.6\times10^{-6}\,K^{-1}$, $\alpha_b=10.1\times10^{-6}\,K^{-1}$ and $\alpha_c=16.3\times10^{-6}\,K^{-1}$, and for $MgTi_2O_5$ $\alpha_a=2.3\times10^{-6}\,K^{-1}$, $\alpha_b=10.8\times10^{-6}\,K^{-1}$ and $\alpha_c=15.9\times10^{-6}\,K^{-1}$.[44,45] The microstructure of the solidified slag, as studied in this project, also displayed considerable microcracking (and the crystal structure of the solidified slag is also that of pseudobrookite, with considerable anisotropy of thermal expansion[7]). This is one likely reason for the relatively low thermal conductivity of the solidified slag. Other likely reasons include the relatively high molar mass of the cations in the solidified slag, and that the slag is a solid solution.[43] As with metals, solid solutions of oxides are observed to have considerably lower thermal conductivities than the pure end members.[43]

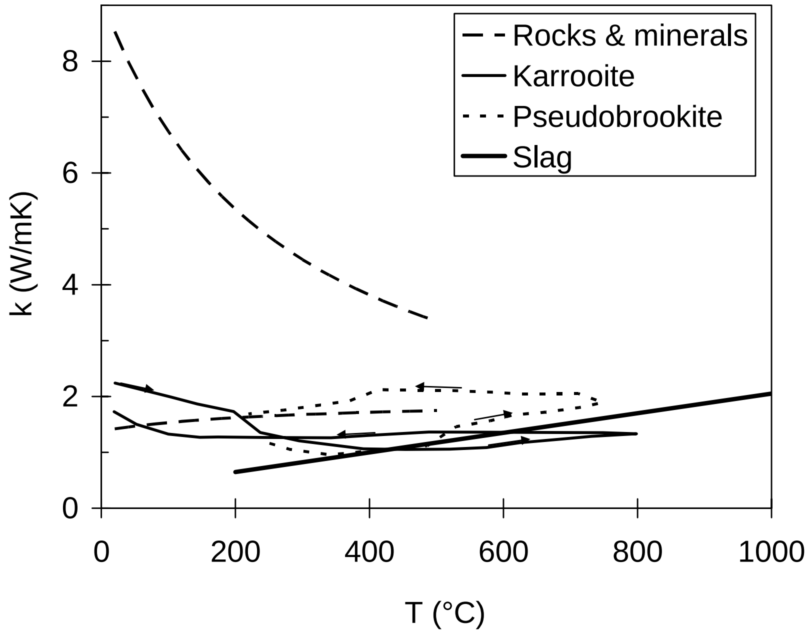

Figure 91 Comparison of the fitted thermal conductivity of the solidified slag (heavy line), with literature data on the range of thermal conductivity of natural rocks[40] (broken line), and synthetic karrooite[44] ($MgTi_2O_5$) and pseudobrookite[45] (Fe_2TiO_5). For the M_3O_5 materials, the arrows indicate the direction of temperature change during the measurements.

4.9 Model verification

The block cooling model was verified against the following information from 18 ton (plant-scale) blocks: (i) the thickness of the crust after primary cooling (18 hours in the pot) and (ii) the surface temperatures of the block after 3 days of cooling under water sprays.

4.9.1 Crust thickness

In Figure 92 the thickness of the block shell after 18 hours of cooling in the pot could be seen clearly because the block fractured directly after being tipped out of the pot. In this instance the thickness of the shell is of the order of 300 mm to 320 mm. The model predicts the liquidus and solidus contours for a similar sized block - cooled for an equal duration in the pot - to be 371 mm and 276 mm from the round end of the block surface respectively (Figure 93). The actual crust thickness is therefore close to halfway between the liquidus and solidus contours.

Evidence was found in both the industrial and pilot trials of the formation of a gap between typical dome and ball structures within the block (Figure 94(c)). This is thought to be a direct result of shell formation during primary cooling, followed by the tipping action and further shrinkage during subsequent cooling. The measured dome thickness of these blocks was around 400 mm. Unfortunately the primary cooling duration of these blocks are unknown. It is not clear why the gap forms in some instances and not in others.

Figure 92 Internal structure of a partially solidified block, as revealed by failure during tipping after primary cooling in the pot.

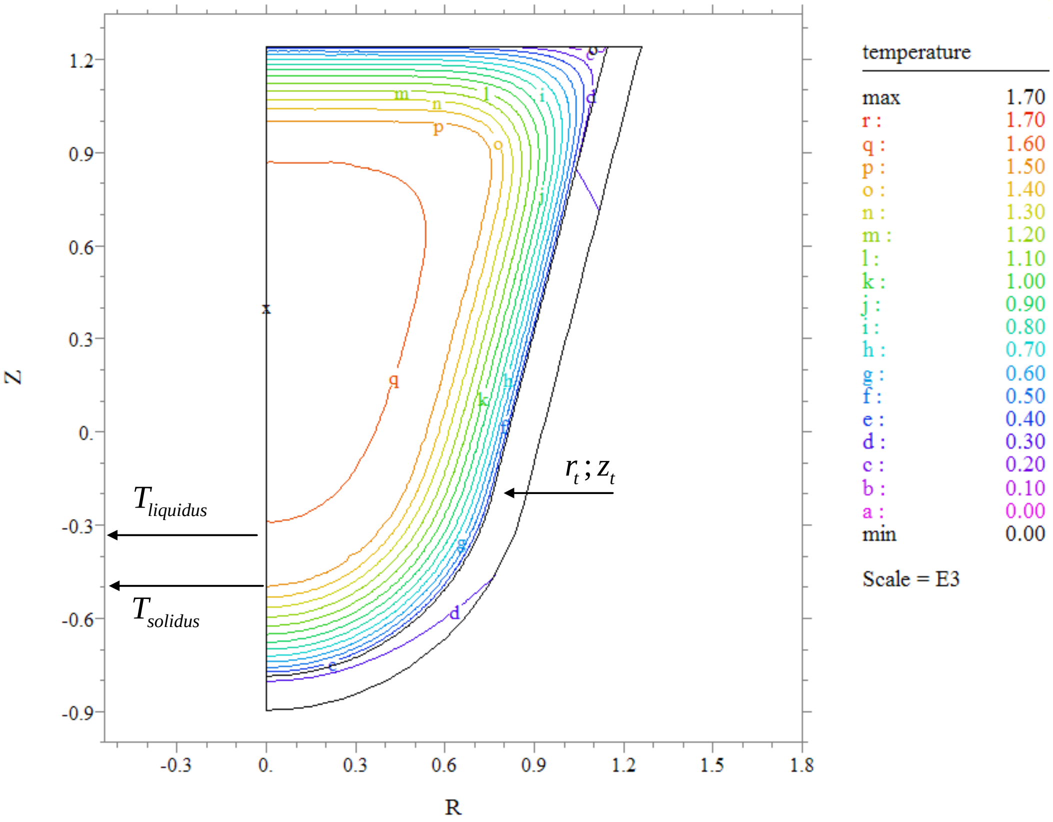

Figure 93 Temperature contours (scale in thousands of ˚C) of an 18 t block after 18 hours primary cooling (in pot).

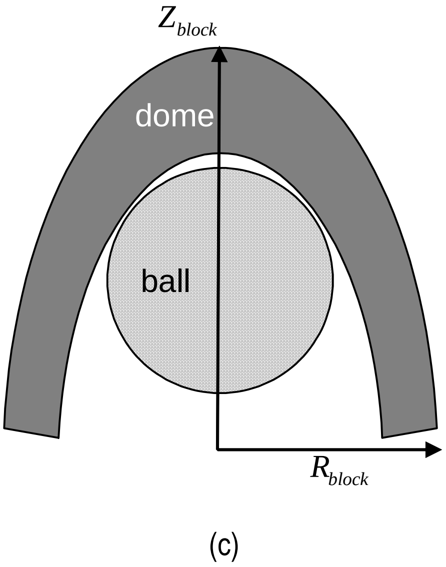

Figure 94 Internal macro structure of solidified blocks showing the shell formation during primary cooling and the ball formation in the centre of the block: (a) and (b) blocks weighing approximately 18 ton; (c) sketch illustrating the ball and dome macro structures which are displayed in (a) and (b).

4.9.2 Surface temperatures

The surface temperatures of the two blocks L1R9 and L2R11 (discussed in Part 2) were measured with an optical pyrometer when the spray water was stopped after 3 days. These temperatures are shown in Figure 95 together with the model predicted surface temperatures of the block surface. The average surface temperature was calculated from two to four actual measurements taken below the 0.5 m height. This band corresponds with the 0.6 m to 1.2 m marks on the Z-axis of Figure 93 and Figure 96. The model predictions correlate well with the actual temperature measurements.

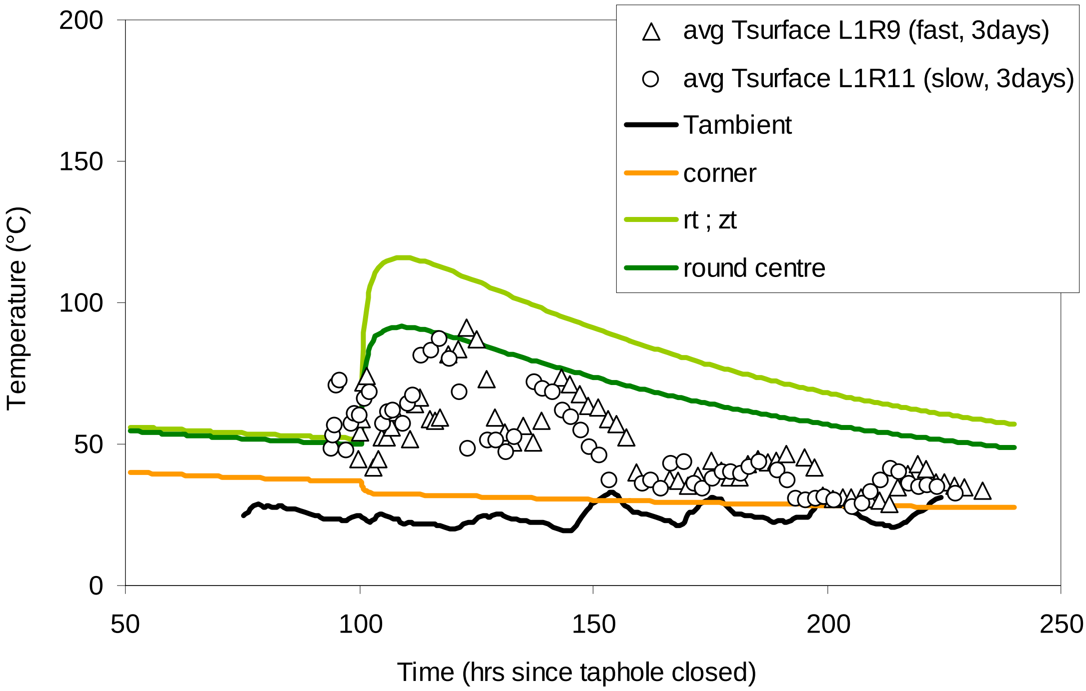

Figure 95 Surface temperatures of two 18 ton blocks. Symbols represent actual measurements while lines represent model predictions.

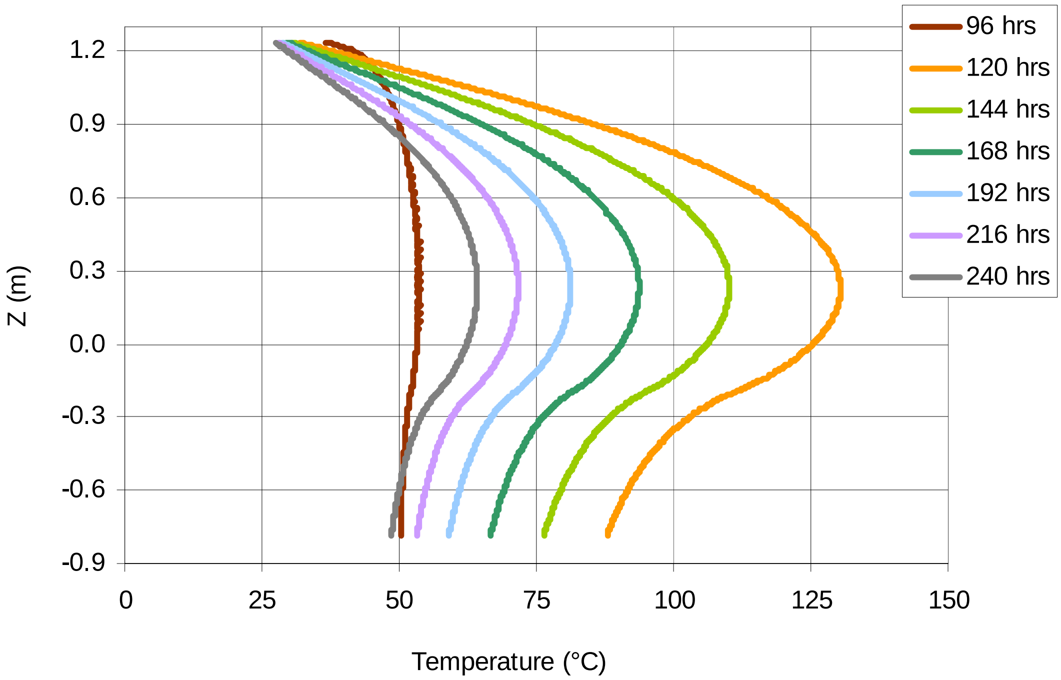

Figure 96 Surface temperatures of an 18 ton block; times are expressed relative to the time of closing the taphole.

4.10 Implication for large scale operations

4.10.1 Solidification

Following primary cooling the block is tilted out of the pot, by means of an overhead crane. The block is then picked up, and driven by a front end loader to be placed in the block yard. As soon as the front end loader is out of the range of the water sprays, the water is turned on. In view of this relatively crude handling method the thickness, strength and toughness of the crust at the end of primary cooling are important. Failure of the crust and subsequent trapping of water underneath liquid slag results in powerful hydrogen or steam explosions – an occurrence which must be avoided to prevent serious injury and/or damage.

It is of interest to test whether this potentially unsafe situation could be eliminated by cooling the block in the pot for longer periods. In Figure 97 the growth of the shell along the vertical centre line of the block (z-axis) for the flat and round ends of the block is shown. The last fully liquid node disappears between 52 and 53 hours of cooling. At this point in time the mushy zones (partially solidified slag, between liquidus and solidus temperatures), which are growing from the top and bottom, meet. The last mushy zones disappear between 92 and 93 hours. The solidification rates of a pot-cooled block are compared with those of water and air cooled blocks in Figure 98: the water-cooled block undergoes final solidification between 90 and 91 hours. Other than this relatively small difference in solidification time, the blocks solidify identically.

The shrinkage of the diameter of the liquid core along the block height (z-axis) can be described by equation (24). Similarly the diameter of the mushy zone can be described by equation (25). In both instances d is in metre and t in hours, counting from the time of closing the taphole.

$$d_{liquid} = -2.413\times10^{-5}t^{3} + 1.664\times10^{-3}t^{2} - 5.696\times10^{-2}t + 1.951 \tag{24}$$

$$d_{mushy} = -2.041\times10^{-6}t^{3} + 2.101\times10^{-4}t^{2} - 2.135\times10^{-2}t + 1.847 \tag{25}$$

From Figure 99 – which zooms in on the first half hour after tapping - the initial crust growth on the flat surface of the block is rapid, but re-melts after approximately 100 seconds. Similar behaviour is not shown by the round end of the block. The inverse resistances to heat flux at the block's horizontal surface ($h_{convection} + h_{radiation}$) and inclined surface ($\frac{k_{pot}}{pot\,thickness}$) are shown in Figure 100. At the horizontal surface the heat flux conductance (that is, the inverse of the thermal resistivity) is initially high at 406 W/m^2˚C, declining to 64 W/m^2˚C after 1 hour. On the inclined surface the conductance remains in the range 300 – 450 W/m^2˚C for the first hour of cooling. The conductance of the horizontal surface drops below this range after only 15 seconds following closure of the taphole. This can be explained by to the large contribution of radiation to the heat flux on the horizontal surface and the rapid formation of a dark crust on this surface, limiting radiation. This then opens the opportunity for the horizontal crust to be re-melted by the molten mass underneath.

On closer inspection the same phenomenon does occur at the slag-pot interface as shown in Figure 100(a) and (b): the conductance starts off around 300 W/m^2˚C, increases to approximately 440 W/m^2˚C after 100 seconds and then decreases to below 350 W/m^2˚C after 1 hour of closing the taphole. In this instance the reheating manifests in the steel pot shell.

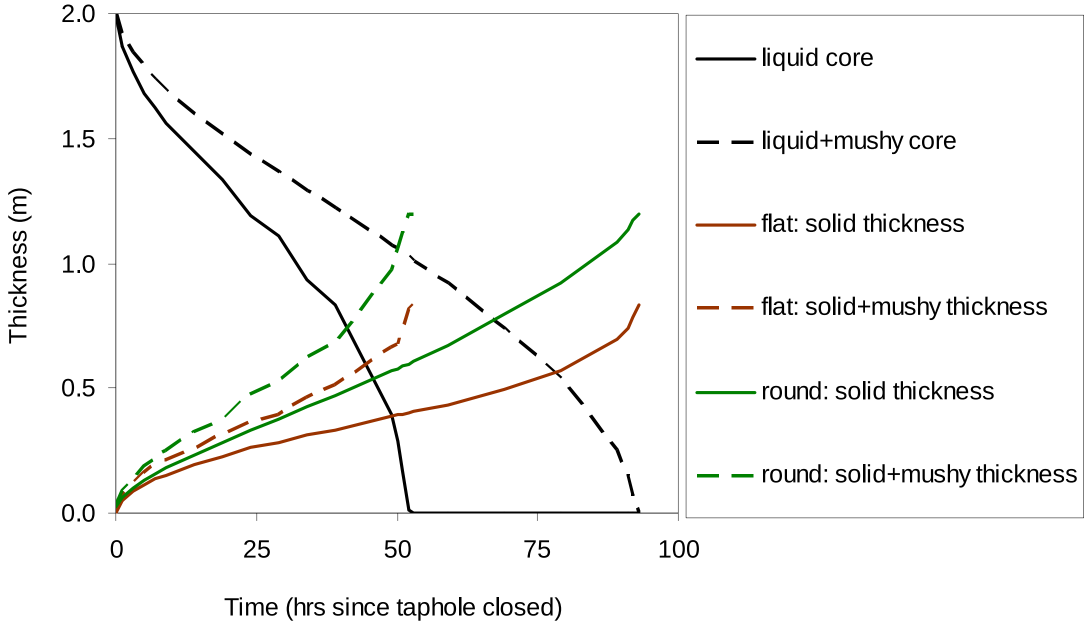

Figure 97 Remaining liquid core and shell thicknesses of a slag block cooling in a pot up to complete solidification.

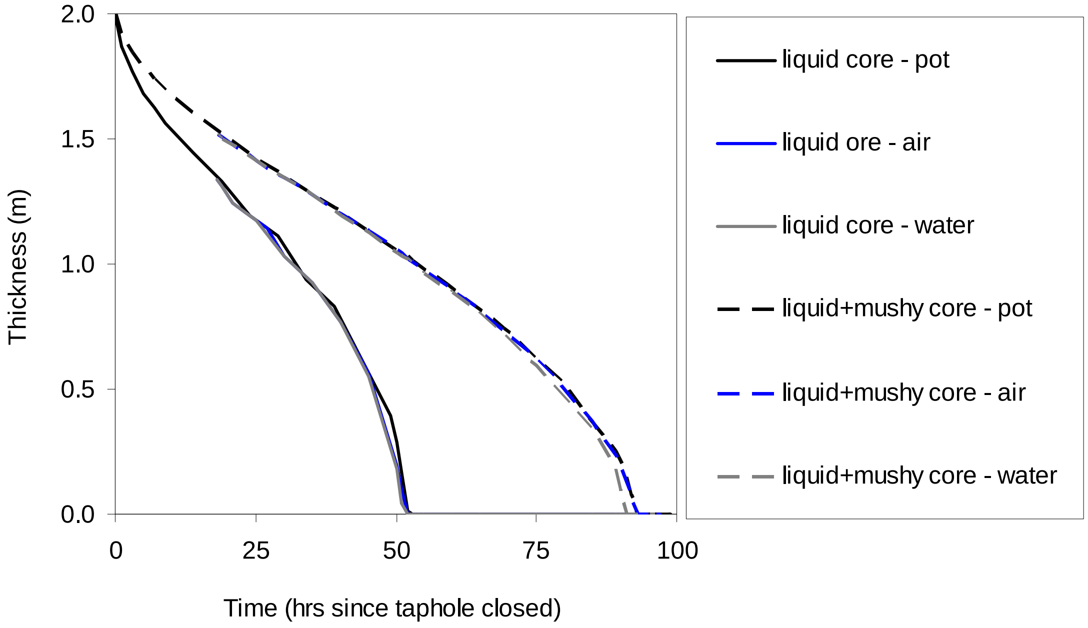

Figure 98 Comparison of the remaining liquid and mushy cores, for slag blocks cooled in the pot, in air and with water cooling.

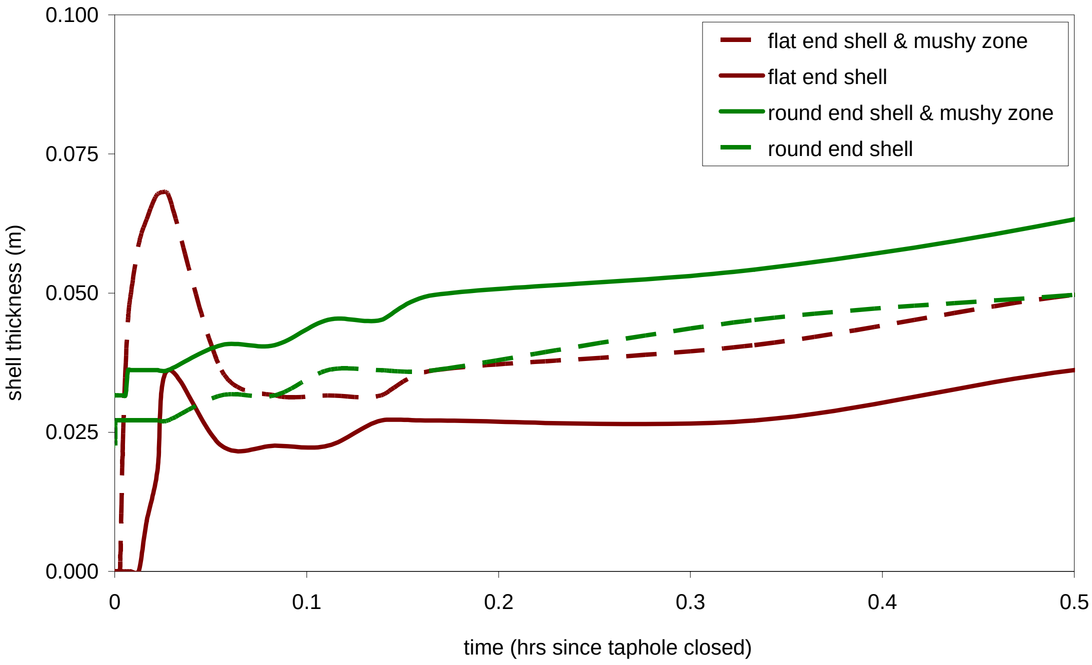

Figure 99 Shell growth of the slag block for the first half hour of cooling in a pot.

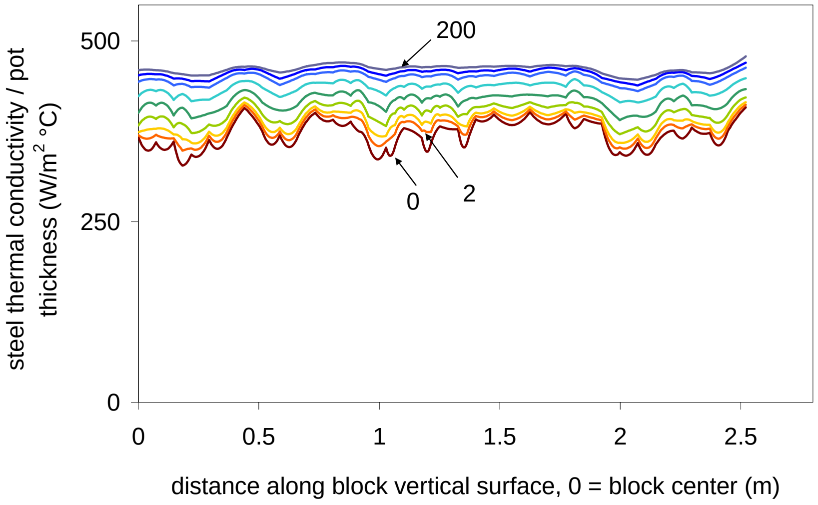

(a)

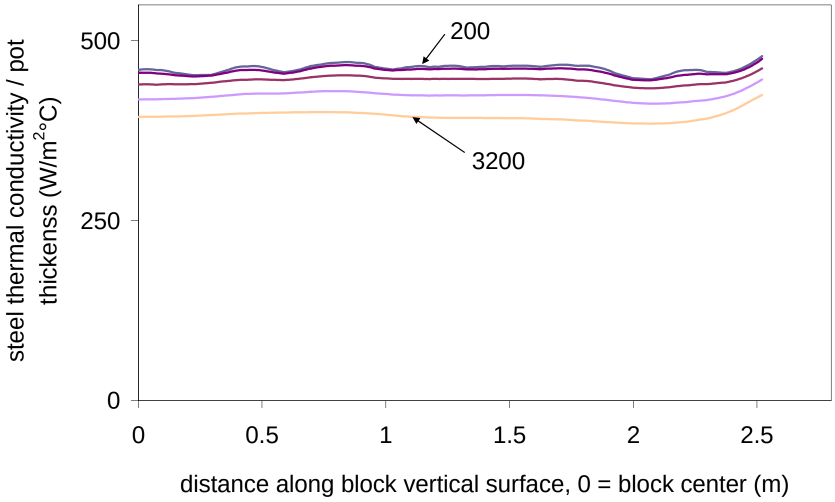

(b)

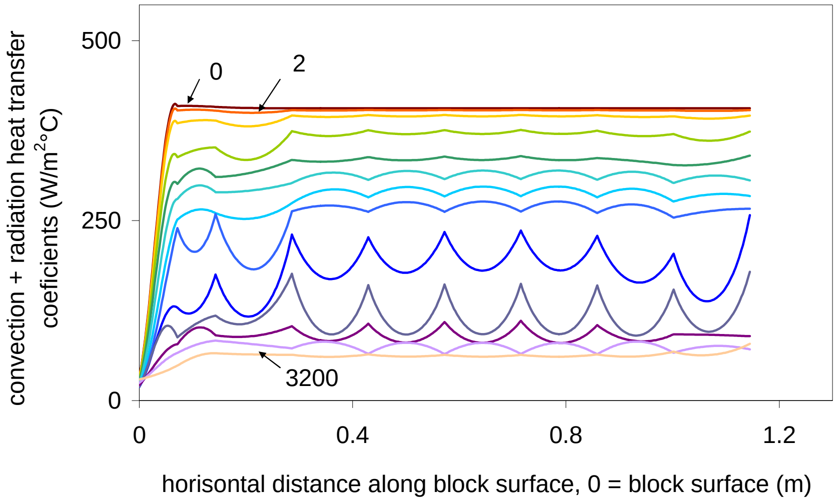

(c)

Figure 100 Thermal conductance for horizontal and inclined (vertical) surfaces. The units of the values within the above graphs are in seconds, counting from closing of the taphole. Time increments run according to the series 0, 2, 4, 8, 16, 32, 64, 100, 200, 400, 800, 1600, 3200

4.10.2 Surface temperatures

Although the solidification rates do not differ between the various cooling methods, the block surface temperatures do – as shown in Figure 101. With continuous water cooling the surface temperatures immediately fall below 70˚C and continue to fall below 50˚C after 10 days. The surface of an air-cooled block remains in the temperature range where decrepitation typically occurs for 3 to 4 days. Only after 7 days is the whole surface below 100˚C.

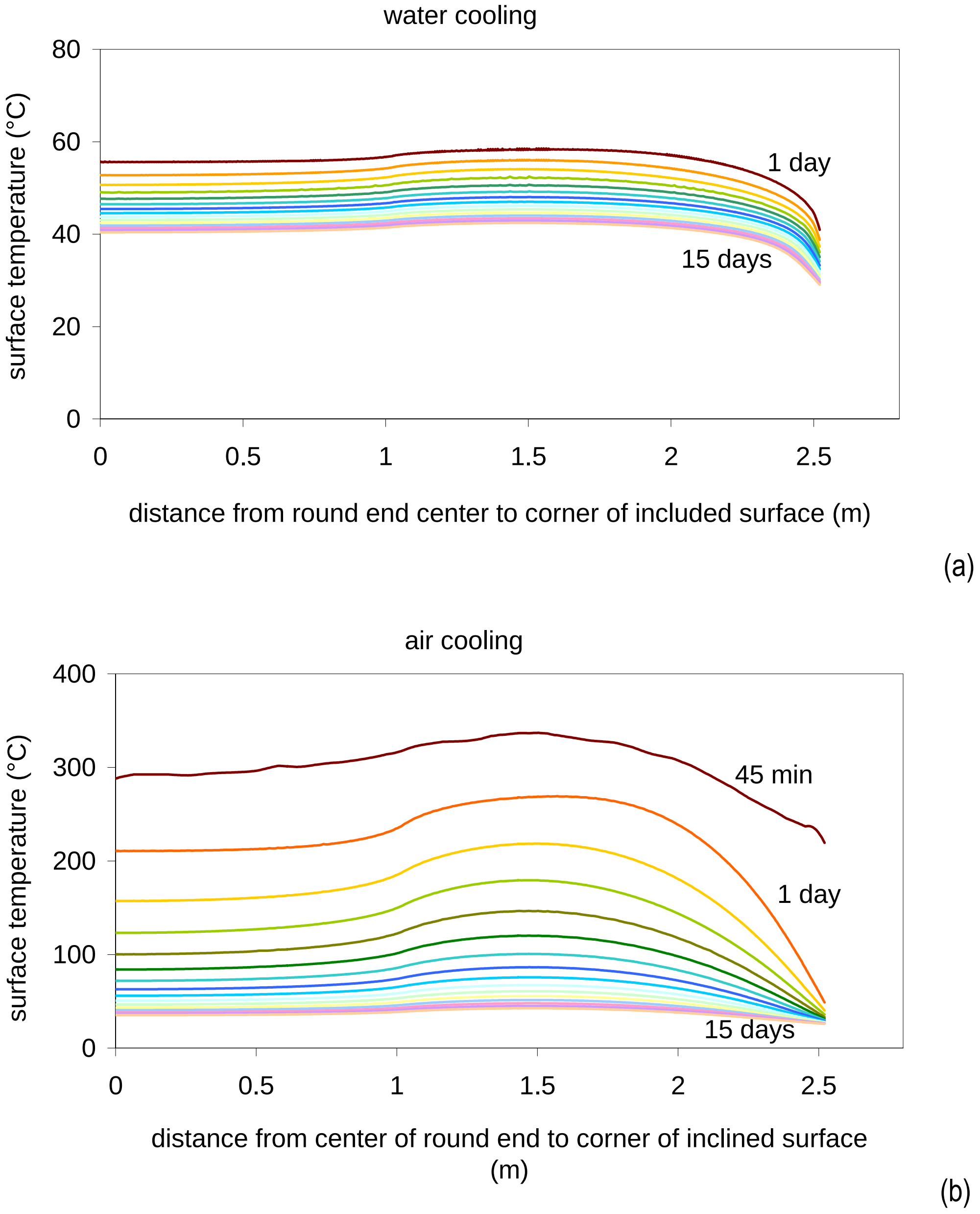

Figure 101 Surface temperatures along the inclined surface of the block for (a) cooling in water and (b) cooling in air. 0 denotes the block centre at the round end of the block, with the corner between the horizontal and inclined surface the furthest point.

The two dimensional heat transfer effects occurring at the corner between the horizontal and inclined surfaces show clearly in the steep temperature gradients of Figure 101. These temperature gradients are the likely cause of breakage of these corners as is typically seen in the block yard (Figure 102). Although still steep, the gradient for the water cooled block is an order of magnitude smaller than that of the air cooled block. Sufficiently water-cooled blocks should hence be less prone to breaking corners. Materials handling difficulties caused by such breaking behaviour can therefore be reduced by ensuring sufficient cooling water.

From previous work[5], decrepitation typically occurs at temperatures in the low hundreds of degrees Celsius. Evidence was furthermore given in section 2 showing that phase transformations occur at temperatures as low as 100˚C. From Figure 103(a) the time that the inclined surface spends in the decrepitation/transformation temperature range is sufficiently long for these two oxidation mechanisms to occur simultaneously on different areas of the surface of one block. Should such oxidation mechanisms influence the mechanical strength of the slag, it can be expected that the comminution equipment of the slag processing plant would receive, and produce, a wide variation in the particle size distribution. This would lead to particle size distribution behaviour as displayed by the two plant blocks which were cooled under water for 3 days only (Figure 31). The actual differences in structure leading to such differences in breaking behaviour could not be pinpointed in this study. Microstructural and microtoughness studies on a very fine scale would be required to provide answers to this question.

Figure 102 Photograph of a 17-18 ton slag block showing typical breaking off of the corner between the horizontal and inclined surfaces. To the left of the broken-off corner decrepitated material has formed.

The internal temperature gradient within the block along the line from the block centre to the point on the surface where the spherical and conical sections meet (points (0;0 and $r_t ; z_t$ respectively on Figure 97), are shown in Figure 104(a) and (b). For a given time the water cooled block (dotted lines) is at lower internal temperatures than the air cooled block (solid lines). Closer to the surface the temperature gradient of the water cooled block is steeper – even more so in the initial cooling stages. The steepest temperature gradients are experienced at the surface of a water cooled block during the first hour of cooling with temperature differences of up to 12.5 ˚C/mm (Figure 104(b)). Such temperature gradients are likely the cause of “peeling” (spalling) on the block surface (visible in Figure 102). The thickness of such spalled material is typically in the range 2-15 mm. The thermal gradient across this distance on the shell of a water cooled block ranges between 9 to 13˚C/mm. Stresses resulting from these temperature gradients are thus likely to exceed the fracture stress of the slag[7], causing crack initiation.

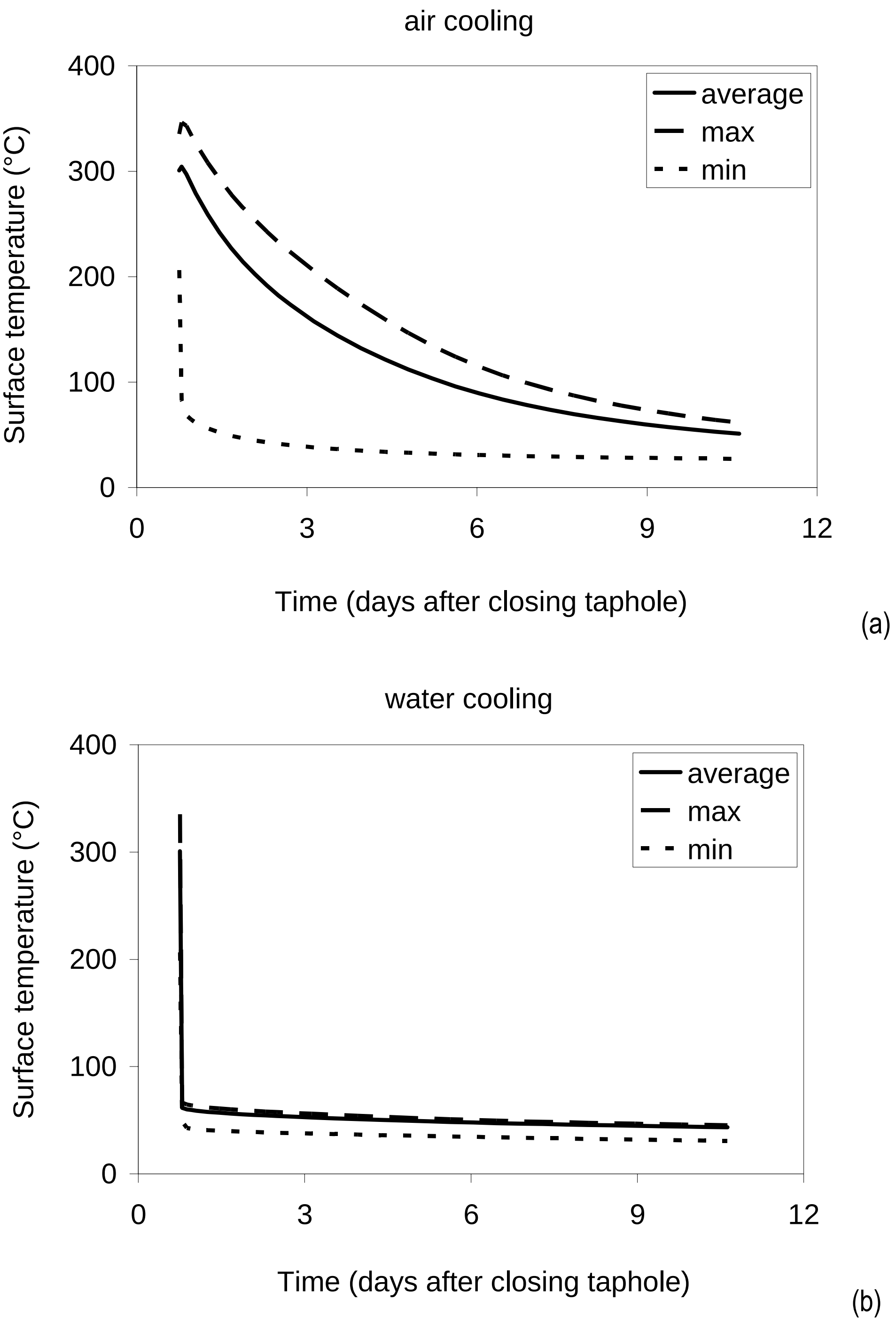

Figure 103 Average surface temperatures of (a) air and (b) water cooled blocks. Maximum and minimum surface temperatures are shown with dotted lines.

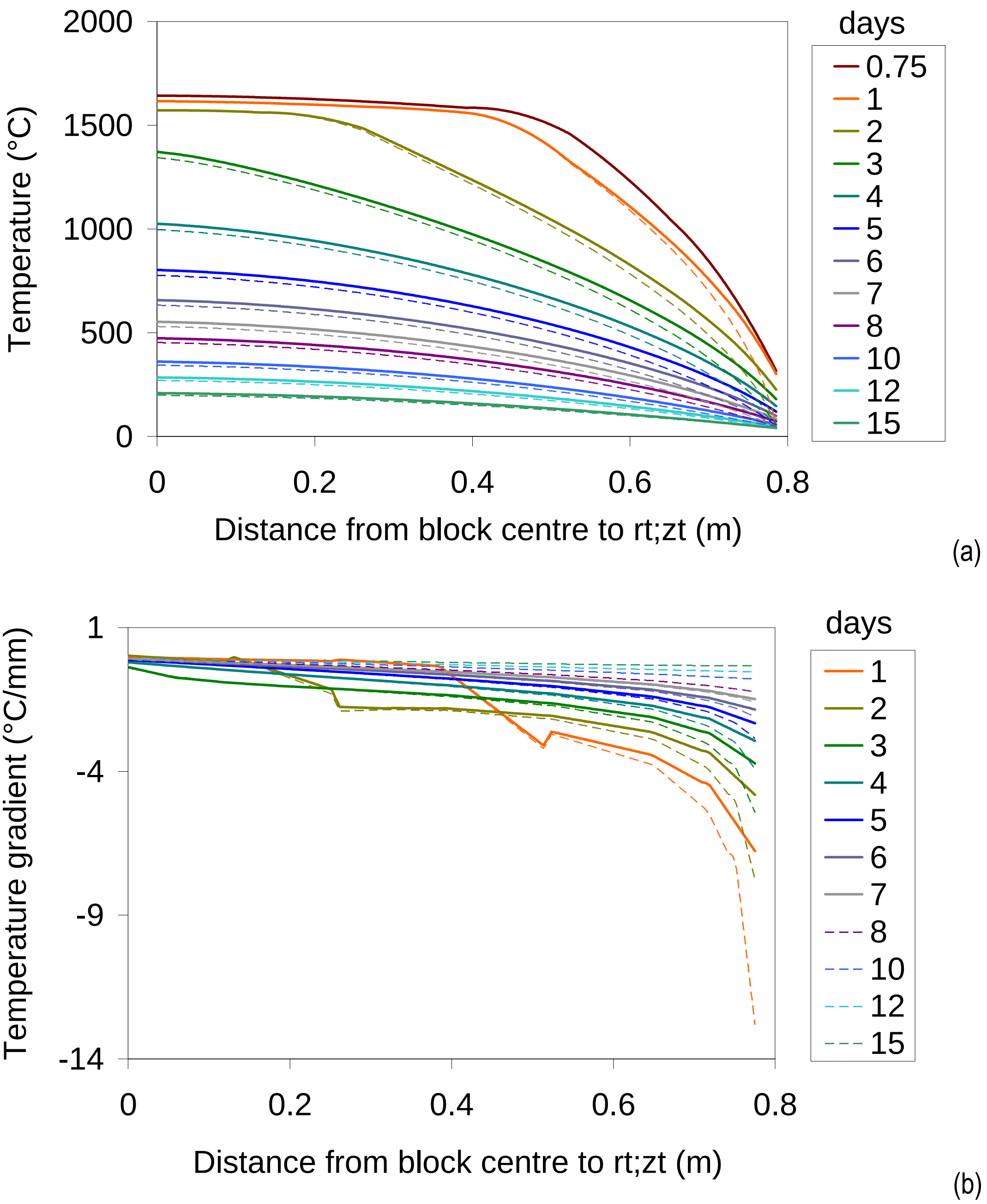

Figure 104 Internal temperature gradient of an air and water cooled block along the line from the centre point of the block to the transition point between the spherical and conical section of the block – points (0;0) and ($r_t ; z_t$) respectively on Figure 93. Solid lines indicate air cooling while dotted lines indicate water cooling.

Further with regard to surface temperatures: premature closure of the spray cooling water was observed (during both pilot and plant trials) to be followed by reheating of the block surface. The model-predicted surface temperatures of an industrial size (17-20 ton) slag block one hour after closing the cooling water are shown in Figure 105, where the period of water cooling was varied from 1 to 10 days. The initial surface temperature immediately after closing the cooling water is shown by the black line in Figure 105. After one day of water cooling, the entire block surface reheats to above 200 ˚C within 1 hour of closing the cooling water. After 3 days of water cooling the surface reheats to above 100 ˚C one hour after closing the cooling water.

Surface reheating reduces notably with increasing water cooling time, but does not disappear completely, even after 10 days of water cooling when a temperature increase of 6 ˚C is predicted for the corner of the block (46 ˚C immediately after closing the water, increasing to 52 ˚C after one hour of air cooling).

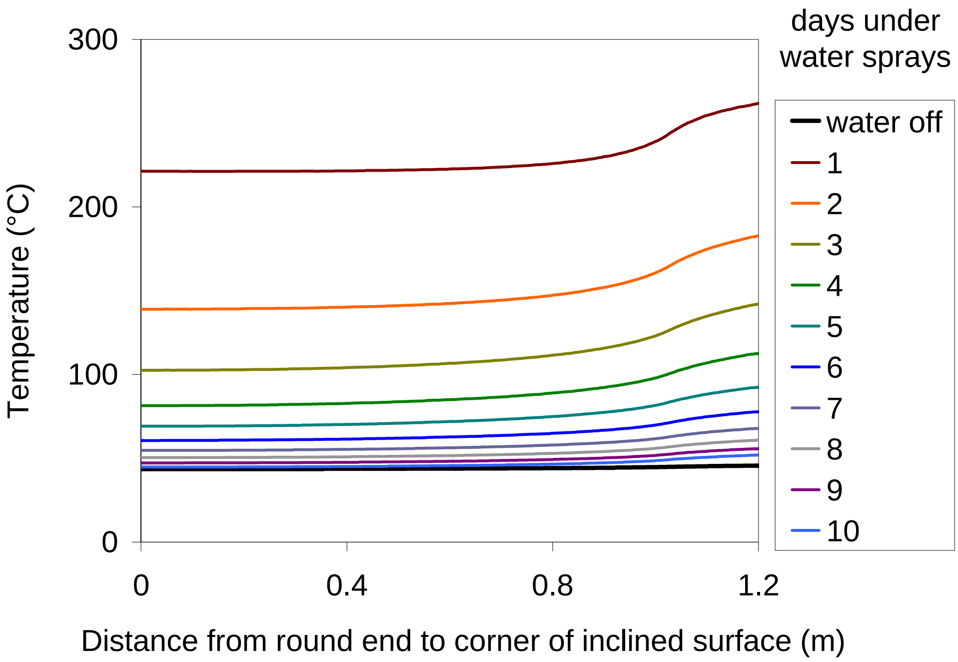

Figure 105 Surface temperatures of a slag block cooled between 1 and 10 days under water and allowed to re-heat for 1 hour.

4.10.3 Internal temperatures

From time to time, it is required (on the industrial plant) to break and crush the slag blocks before the normal cooling period of 10 days has elapsed. In these circumstances it is important - from a safety point of view - to note that the blocks solidify completely after 90 to 93 hours (close to 4 days) after closing the taphole. There is hence no danger of liquid material escaping. However, if hot internal material is exposed by breaking, oxidation is expected. To limit such oxidation effects on the newly exposed inner surfaces of a block after breaking, the inner temperatures of the block as a function of time must hence be known.

A series of contours comparing the isotherms of a water and air cooled block on a daily basis from 1 to 10 days of cooling is given in Appendix 5.9. From these and Figure 104(a) the centre of the block is still at 200˚C even after 15 days of cooling. At this stage the temperature gradient from the block centre to surface ranges from 0 to 0.3 ˚C/mm. From the previous paragraphs it is clear that the solidified slag crust is the rate limiting step in block cooling. Hence, with the temperature gradient over the block centre to surface controlling the rate of cooling, 0.3 ˚C/mm is a small driving force for cooling.

From extrapolation of the cooling rate at 15 days the block centre will reach 100˚C after 25 days of cooling. From Part 1 and 2 low temperature oxidation (≤100 ˚C) does occur and appears to negatively affect the particle size distribution of the slag. It therefore unlikely that exposure of the block centre to air while still at temperatures above 100 ˚C can be prevented for practical cooling programmes. However, it would be beneficial to promote rapid cooling of the fragments which are produced by primary breakage, for example by not packing the fragments directly on top of one another, but rather spreading these out in a single layer. The time which would be required for such (natural) cooling of primary crushing fragments was not estimated in this study, but a similar numerical cooling model (to the one used here for slag solidification) could be used for this purpose.

4.11 Conclusions

From the model calibration work the best-fit thermal conductivity for titanium dioxide slag is shown in Figure 90 and given by equation (23). The values of the constants in the latter equation are relatively insensitive to errors and assumptions in the calculated liquidus and solidus temperatures – except when the liquidus temperature drops by 5%. From plant experience, the probability that the liquidus temperature is higher than the theoretical estimates, rather than lower, is much greater in any case.

Of significance is the fact that final solidification and cooling of the block centre are independent of the cooling method. It is therefore confirmed that the thermal conductivity of the slag (or, more exactly, the thermal resistance of the layer of solidified slag) is the rate determining parameter in the block cooling process.

The surface temperatures of blocks in an industrial set-up will likely be somewhere between the two extremes predicted by the cooling model for water and air cooled surfaces. The efficiency of the water sprays influences the success of large scale water cooling (e.g. block nozzles, wind direction and speed, etc.).

From the Part 1 it was evident that decrepitation is self-sustaining in the sense that where left undisturbed, decrepitated material creates an environment favourable for further decrepitation (refer to tap 59 which ended up with a block yield of 10.8%). An instance of this is found in the industrial plant during primary cooling where the (upper) horizontal surface of the block decrepitates and the fine product accumulates on this surface. The layer of decrepitated material forms a very effective insulation layer which limits heat transfer from this surface. The internal slag temperatures beneath the horizontal surface are therefore expected to be higher than what is predicted by the block cooling model. It is therefore feasible that when the decrepitated layer is removed from this surface when the block is tipped out of the pot, the block has a thinner crust on this surface – and this is the surface which must withstand all handling when moving the block via front-end loader to the block yard. The advantages of preventing or limiting decrepitation during primary cooling are therefore less fines generation and likely a reduction in the probability of block explosions during handling.

In summary, the final particle size distribution of titania slag is predominantly influenced by

(i) The amount of intergranular silicate phases, and

(ii) Oxidation reactions over the full temperature range of cooling

With regard to the silicate glass phases (which originate from both ilmenite and the reductant, and are primarily functions of the orebodies, but which can be influenced to a limited extent by the beneficiation processes upstream of the smelter) the question is whether an increase thereof would limit the growth of the karrooite (M_3O_5) grains. If an increased silicate fraction were to limit the karrooite grain growth, this would most definitely be detrimental to achieving the specified product size distribution (since the smallest dimension of the karrooite grains is already at or below the minimum of the specified product size range). The other extreme possibility would be where the karrooite grains were free to grow, with the intergranular silicate/glass region simply growing in thickness with increased volume fraction of silicates. In this case, fracture of the silicates (during comminution) is expected to increase the proportion of the silicates which report to the fine slag, causing a decrease in the grade of the fine slag (and a likely increase in the proportion of fine slag). Microscopy on samples with a wider range of silicate contents, but similar solidification conditions, would be required to provide answers to these questions.

With regard to oxidation during the cooling stages, it is evident that water cooling limits oxidation. Intense water cooling does unfortunately have advantages and disadvantages. The advantages of intense water cooling are summarized as follows:

- Intense water cooling limits decrepitation - likely due to suppression of the block surface temperatures below 50˚C which slows down the rate of the M_3O_5 to M_6O_{11} oxidation reaction.

- From section 3.7.2 there are indications that intensive water cooling stabilises phases, preventing (or at least limiting) further low temperature (< 100 ˚C) oxidation. Such low temperature oxidation was linked to blocks performing poorly with regards to particle size distribution.

- An additional advantage of a water cooled block is the narrower temperature range over the whole surface which in turn leads to a narrower particle size distribution during processing. This in turn allows narrower equipment settings, which would result in optimum control over particle size distributions.

- Intensive water cooling furthermore reduces the thermal gradient – and resultant stresses – along the inclined surface of the block, which in turn should reduce the occurrence of corner chunks breaking off while cooling in the block yard. Where such breakage does occur, additional and tedious materials handling is required to prevent material losses.

Intense water cooling has the following disadvantages:

- It was found in Part 2 that intense water cooled blocks yielded higher residual coarse fractions. Translated to a production environment this implies higher circulating loads to the mill. Hence the probability for indirect fines generation increases, while total capacity of the mill is also reduced.

- Although the temperature gradient along the inclined surface of the block is less for an intensely water cooled block, a steep temperature gradient exists along the radial axis of the block with intense water cooling. The stresses associated with such temperature gradients promotes "peeling" (2-15 mm thick spalled material) to separate from the block surface. Careful and tedious materials handling is therefore required to prevent material losses.

4.11.1 Proposed further research

Although this study positively links oxidation with the final particle size distribution, the exact mechanism is still unknown. The anisotropic expansion behaviour of the pseudobrookite phase of the slag provides a possible avenue to explain this link. Insight into this mechanism could identify opportunities to further decrease the fraction of the fine slag.

Further insight into these slags can be obtained by studying the composition-oxidation link of these slags by conducting phase analyses on a micro scale, at different positions within the slag block. This study can be further expanded by adding varying cooling environments and rates.

In terms of decrepitation the advantages of water cooling is obvious. The remaining question to answer is whether the benefit from intense water cooling in terms of preventing low temperature oxidation (which was linked to high direct fines generation) and narrower particle size distribution (and hence optimum plant control), is greater than the indirect increase in fines generation due to higher circulating loads to the mill. Since the equipment and process flow used in the experimental work of Part 2 were not representative of the industrial plant, the question can unfortunately not be answered from these results. Practical investigations on the industrial plant would be required to resolve this.